



1 **High frequency, continuous measurements reveal strong diel and seasonal cycling of**
2 **$p\text{CO}_2$ and CO_2 flux in a mesohaline reach of the Chesapeake Bay**

3

4

5 **A. Whitman Miller^{1*}, Jim R. Muirhead¹, Amanda C. Reynolds¹, Mark S. Minton¹ and Karl**
6 **J. Klug¹**

7 ¹Smithsonian Environmental Research Center, 647 Contees Warf Road, Edgewater, MD 21037
8 USA

9

10 Corresponding author: A. Whitman Miller (millerw@si.edu)

11 **Key Points:**

- 12 • Automated $p\text{CO}_2$ measurements capture daily cycles and anomalous events in estuaries
13 where $p\text{CO}_2$ changes rapidly and across a wide range.
- 14 • Rhode River is net autotrophic (Dec–May), net heterotrophic (Jun–Nov), net ecosystem
15 production is near balanced annually, but can reverse status during a single day.
- 16 • Year-round continuous measurements reveal that $p\text{CO}_2$ and CO_2 flux are mediated by
17 temperature effects on biological activity and are inverse to the physical solubility of
18 CO_2 .



19 **ABSTRACT**

20 We estimated hourly air-water gas transfer velocities (k_{600}) for carbon dioxide in the Rhode
21 River, a mesohaline subestuary of the Chesapeake Bay. Gas transfer velocities were calculated
22 from estuary-specific parameterizations developed explicitly for shallow, microtidal estuaries in
23 the Mid-Atlantic region of the United States, using standardized wind speed measurements.
24 Combining the gas transfer velocity with continuous measurements of $p\text{CO}_2$ in the water and in
25 the overlying atmosphere, we determined the direction and magnitude of CO_2 flux at hourly
26 intervals across a 3-year record (01 July 2018 to 01 July 2021). Continuous year-round
27 measurements enabled us to document strong seasonal cycling whereby the Rhode River is net
28 autotrophic during cold-water months (Dec–May), and largely net heterotrophic in warm-water
29 months (Jun–Nov). Although there is inter-annual variability in CO_2 flux in the Rhode River, the
30 annual mean condition is near carbon neutral. Measurement at high temporal resolution across
31 multiple years revealed that CO_2 flux can reverse during a single 24-hour period. $p\text{CO}_2$ and CO_2
32 flux are mediated by temperature effects on biological activity and are inverse to temperature-
33 dependent physical solubility of CO_2 in water. Biological/biogeochemical carbon fixation and
34 mineralization are rapid and extensive, so sufficient sampling frequency is crucial to capture
35 unbiased extremes and central tendencies of these estuarine ecosystems.

36

37 **1. Introduction**

38 Understanding the air-sea exchange of gases and establishing methodologies for accurate
39 measurements has been a decades-long focus of atmospheric scientists, oceanographers, and
40 biogeochemists seeking to understand interactions between oceans and the atmosphere and how
41 these interactions contribute to the global carbon cycle (Broecker et al., 1979; Wanninkhof,
42 1992, 2013). Coastal oceans and estuaries are ecosystems of interest for understanding the
43 complex nature and contribution of the land-sea interface to lateral mass transport of carbon
44 (Abril & Borges, 2005; Cai & Wang, 1998; Frankignoulle et al., 1998; Song et al., 2023) but also
45 with respect to the role these ecosystems play as both atmospheric CO_2 sources and sinks (Abril
46 & Borges, 2005; Chen et al., 2020; Dai et al., 2022; Jiang et al., 2008). The exchange of carbon
47 dioxide, methane, and other greenhouse gases between Earth’s atmosphere and inland waters,
48 estuaries, coastal oceans are well-documented but not necessarily fully quantified (Abril &
49 Borges, 2005; Cai, 2011; Laruelle et al., 2017; Raymond & Cole, 2001; Raymond et al., 2013;



50 Van Dam et al., 2019). CO₂ evasion from estuaries alone has been estimated at 15–17% of the
51 total input from oceans to the atmosphere (Chen et al., 2020; Laruelle et al., 2017), indicating the
52 regional and global significance of estuaries (Bauer et al., 2013; Frankignoulle et al., 1998; Jiang
53 et al., 2008). Yet, there is still great uncertainty surrounding the true net contributions of coastal
54 oceans, estuaries, and inland water bodies to the atmospheric loading of greenhouse gases
55 (Borges, 2005; Chen et al., 2020; Herrmann et al., 2020; Joesoef et al., 2015; Laruelle et al.,
56 2017; Raymond et al., 2013; Van Dam et al., 2019).

57

58 To better understand the effects of estuaries on atmospheric greenhouse gas exchange and
59 accumulation, it is imperative that we understand their capacity and function as carbon sources
60 and sinks and ultimately how estuaries factor into the planet's overall global carbon budget
61 (Herrmann et al., 2020; Laruelle et al., 2017; Van Dam et al., 2019). Many attempts to
62 characterize CO₂ flux in estuaries and nearshore oceans (Chen et al., 2013; Herrmann et al.,
63 2020; Rosentreter et al. 2021), have relied on direct measurements using floating domes, tracer
64 gases, or more recently eddy covariance methods (Laruelle et al., 2017; Van Dam et al., 2019).
65 Because flux measurements are time intensive, they tend to be temporally and spatially limited
66 (Herrmann et al., 2020; Klaus & Vachon, 2020). Leveraging direct flux measurements to derive
67 accurate gas transfer velocity constants (k_0 , the velocity of gas crossing the air-water boundary)
68 enables models to be parameterized to estimate k_0 and compute gas flux. Thus, correlative
69 models that incorporate contemporaneous environmental measurements such as wind and/or
70 water velocity, factors that affect turbulence at the air-water interface and promote gas exchange,
71 have aided in the widespread accumulation of gas flux estimates (Raymond & Cole, 2001; Van
72 Dam et al., 2019; Wanninkhof, 2014). Gas transfer velocity constant models vary according to
73 the habitat/system being observed and chemical, physical, and biological factors present in each
74 (e.g., lakes, rivers/streams, estuaries, and oceans; Herrmann et al., 2020; Ho et al., 2016;
75 Raymond & Cole, 2001; Van Dam et al., 2019; Wanninkhof, 1992). To reduce uncertainty of
76 computed gas fluxes, it is critical that the appropriate k_0 models are matched to a targeted
77 ecosystem.

78

79 Coastal oceans and estuaries are exceptionally complex, frequently characterized by their relative
80 shallowness and how their freshwater inputs (riverine, surface, and groundwater) mix with salt



81 water (Chen et al., 2020). High nutrient and pollutant loading, due to urbanization and
82 eutrophication by humans, also have important effects on estuaries and coastal oceans (Freeman
83 et al., 2019). High spatial and temporal variability are hallmarks of estuaries.

84

85 Here we present a 3-year data set that combines high frequency (1-min interval) measurements
86 of dissolved and atmospheric CO₂ with co-located and continuous measurements of salinity,
87 water temperature, and wind velocity recorded at the Smithsonian Environmental Research
88 Center (SERC) dock, in the Rhode River, Maryland. To estimate hourly, daily, seasonal, and
89 annual CO₂ flux rates, we applied a CO₂ gas velocity constant model developed by Van Dam et
90 al. (2019) for the New River, North Carolina. This model is expressly designed for application to
91 shallow, well-mixed, microtidal estuaries located in the Mid-Atlantic coast of the United States.

92

93 In the Rhode River, we find that CO₂ flux reverses itself daily for part of the year (June–
94 November) yielding some days that are characterized as a net sink (net autotrophic) and others
95 that are a net source (net heterotrophic). From December to May diel cycling is minimal and the
96 river is almost exclusively a net sink, autotrophic both day and night. Finally, although CO₂ flux
97 is pronounced but variable across seasons, the net CO₂ flux of the Rhode River annually is near
98 neutral.

99

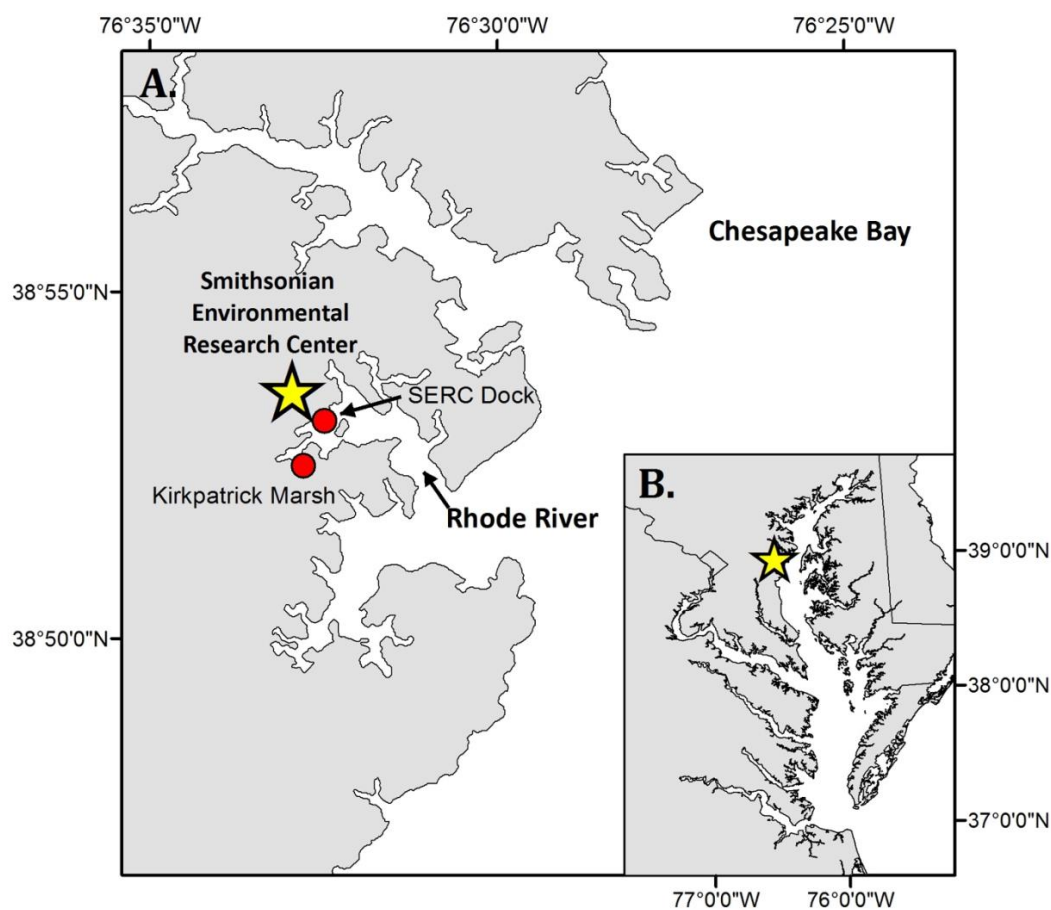
100 **2. Methods**

101 2.1 Study Location

102 The Rhode River is a tributary and sub-estuary of the Chesapeake Bay, a drowned river valley,
103 coastal plain estuary (Fig. 1). The Rhode River has been studied extensively by SERC staff and
104 colleagues for over 4 decades: nutrient chemistry (Jordan & Correll, 1991; Jordan et al., 1991),
105 phytoplankton ecology (Gallegos et al., 2010), color dissolved organic matter distribution
106 (Tzortziou et al., 2008; Tzortziou et al., 2011), and more recently, modeling of dissolved organic
107 carbon (DOC) input from freshwater and tidal marsh sources (Clark et al., 2020). Located on the
108 Bay's northwestern shore (38°52'N, 76°32'W), the Rhode River is bounded at its head by Muddy
109 Creek, its primary source of freshwater, and at its mouth by the mainstem of the Chesapeake
110 Bay. The Rhode River is a shallow (mean depth = 2 m, max depth = 4.1 m), mesohaline (0 to 18
111 ppt), well-mixed, eutrophic tributary with a length of approximately 5 km; its surface area is



112 approximately 500 ha with a shoreline perimeter of 39 km (Breitburg et al., 2008; Clark et al.,
113 2018). A 21-ha tidal marsh (Kirkpatrick Marsh) fringes the estuary at the mouth of Muddy Creek
114 (Fig. 1). Tides are semi-diurnal with a mean amplitude of approximately 30 cm, but water height
115 can be strongly affected by wind and weather events. Muddy Creek is the main freshwater source
116 of the Rhode River and has a maximum flow rate of $10.42 \text{ m}^3 \cdot \text{s}^{-1}$ and mean flow rate $0.18 \text{ m}^3 \cdot$
117 s^{-1} (mean flow = $15,552 \text{ m}^3 \cdot \text{d}^{-1}$; Clark et al., 2020; Clark et al., 2018; Jordan et al., 1986). The
118 mean daily volume of freshwater inflow from Muddy Creek is approximately 0.5% of the mean
119 daily tidal exchange volume, based on the Rhode River's area and mean tidal amplitude. Thus,
120 the Rhode River is not considered a river-dominated estuary. However, Gallegos et al. (1992)
121 observed that occasional freshets emanating from the Susquehanna River, the source of 55% of
122 all freshwater input to the Chesapeake Bay (U.S. Geological Survey, 2023), whose mouth lies 45
123 nautical miles (nm) up bay from the Rhode River, can cause abrupt changes in salinity and
124 nutrient loading in the Rhode River, resulting in predictable phytoplankton blooms. Although the
125 Rhode River is a model ecosystem that has been studied intensively for several decades across
126 many dimensions (Clark et al., 2018; Correll et al., 1992; Gallegos et al., 1992; Jordan et al.,
127 1991; Rose et al., 2019), no work to date has expressly characterized the nature and dynamics of
128 CO_2 flux with the atmosphere.



129

130 **Fig. 1.** Location of study site on the Rhode River, Edgewater MD (A), on the western shore of
131 the Chesapeake Bay (B). All $p\text{CO}_2$ and related water quality values reported were measured from
132 the SERC dock that extends approximately 75 m from shore on the Rhode River. Red circles
133 indicate location of the dock and a tidal creek that drains the Kirkpatrick saltmarsh (marsh area =
134 21 ha, 1 km up estuary from the dock).
135

136 2.2 In Situ Measurements, Calculated Parameters and Quantities

137 Continuous, automated environmental measurements were made in and above the Rhode River
138 during a 3-year period between 01 July 2018 and 01 July 2021. The purpose of these



139 measurements was to document fluctuations in aqueous $p\text{CO}_2$, on a fine time scale, from which
140 CO_2 flux between the water and atmosphere could be calculated.

141 2.2.1 Aqueous CO_2 ($p\text{CO}_{2\text{water}}$)

142 To measure the CO_2 gradient ($\Delta C = p\text{CO}_{2\text{water}} - p\text{CO}_{2\text{air}}$) between the Rhode River surface waters
143 and its overlying atmosphere, measurements of dissolved and atmospheric $p\text{CO}_2$ were made with
144 a non-dispersive infrared (NDIR) detector. In the case of dissolved gas measurements, water was
145 equilibrated continuously with a spherical falling film equilibrator (Miller et al., 2019). Water
146 from 1 m below the water's surface was pumped and dispersed continuously over a 25.4 cm
147 diameter sphere. The falling film created on the outside of the sphere generates a gas exchange
148 surface where CO_2 in the equilibrator headspace is forced into equilibrium with the water's CO_2
149 content (i.e. mole fraction = $x\text{CO}_2$ ($\mu\text{mol/mol}$)). Water exits the equilibrator via an airtight drain
150 that prevents headspace contamination from surrounding atmospheric air. Headspace gas
151 circulates continuously in a closed loop through the equilibrator, water trap and gas
152 dehumidifier, past the NDIR, and back into the equilibrator. Experimental observations
153 concluded that spherical falling film equilibrators achieve 99% equilibration of CO_2 within 10–
154 15 mins, depending on whether step changes are from low to high or high to low; details of the
155 operation and performance of the falling film equilibrator are described in Miller et al. (2019).
156 Measurements were made at 1-min intervals at a pressure equal to the ambient barometric
157 pressure.

158

159 Measured raw CO_2 mole fractions ($\mu\text{mol/mol}$) were converted to partial pressures (μatm) using
160 equation 1. Minute-over-minute values were averaged to provide hourly means. The mole
161 fractions were then evaluated with corresponding water temperature and salinity measurements
162 following the methodology of Zeebe and Wolf-Gladrow (2001) where saturation vapor pressure
163 of water is calculated according to Weiss and Price (1980) to determine $p\text{CO}_{2\text{water}}$.

164

$$165 \quad p\text{CO}_{2\text{water}} = x\text{CO}_2 \cdot (p - p\text{H}_2\text{O}) \quad (1)$$

166

167 where,

168 $p\text{CO}_2$ = partial pressure of CO_2 of water (μatm)

169 $x\text{CO}_2$ = mole fraction of CO_2 in water ($\mu\text{mol/mol}$)



170 $p = \text{total pressure} = 1 \text{ atm}$

171 $p_{\text{H}_2\text{O}} = \text{saturation vapor pressure of water } (\mu\text{atm})$

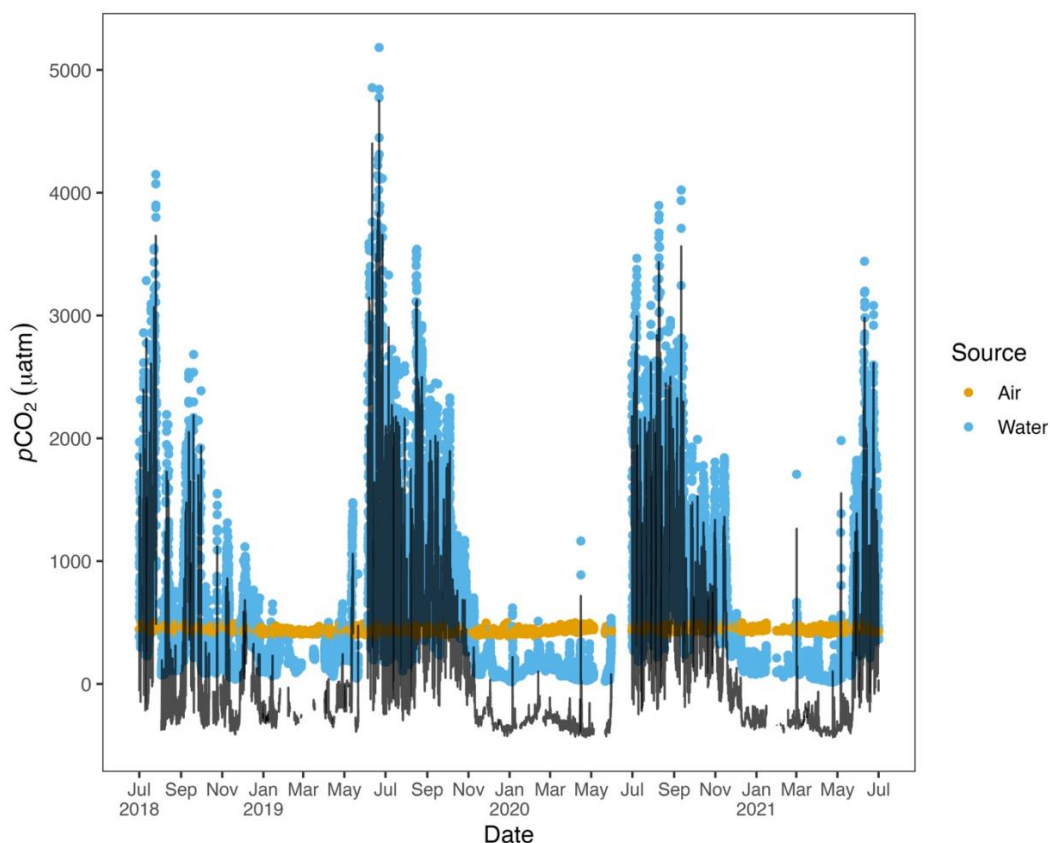
172

173 2.2.2 Atmospheric CO₂

174 Every six hours, the sample gas stream was diverted from the equilibrator to an atmospheric port
175 located approximately 5 m above the pier deck. During atmospheric sampling, 15 1-min interval
176 measurements were made. To account for inaccuracies during the transition period from
177 equilibrator to atmospheric sampling, the final eight measurements were averaged and the first
178 seven were discarded. Similarly, the first 30 measurements following switchover from
179 atmospheric port to equilibrator were discarded, to ensure measurements were not contaminated
180 by any residual atmospheric gas and thus fully equilibrated with water. For these atmospheric
181 measurements, the contribution of the vapor pressure of water to the total atmospheric pressure
182 of the open-air environment was considered negligible (i.e. $p_{\text{H}_2\text{O}} = 0$ and $p = 1$), such that
183 $p_{\text{CO}_2\text{atm}} = x_{\text{CO}_2\text{atm}}$. As such, any potential differences are expected to fall well within the
184 measurement accuracy of the instrument (see below).

185

186 One advantage to using a shared NDIR sensor for aquatic and atmospheric samples is that any
187 minor effects of instrument drift will be reflected in both data streams, as opposed to two sensors
188 that drift independently of one another. Likewise, significant and sustained deviation from
189 typical local atmospheric variability will be captured during atmospheric sampling and can signal
190 the need for recalibration and assist with QA/QC of corresponding data from both streams. A
191 disadvantage of using a common sensor for both dissolved and atmospheric CO₂ measurements
192 is that it results in a mismatch in sampling frequency of the two. With this limitation in mind, we
193 chose a higher sampling frequency for aquatic measurements to better describe the inherently
194 higher variability in dissolved CO₂ in water versus that in the atmosphere (Fig. 2).



195

196 **Fig. 2.** Hourly $p\text{CO}_{2\text{water}}$ (blue) and $p\text{CO}_{2\text{air}}$ (goldenrod) values from 01 July 2018 to 01 July
 197 2021. The air-water CO_2 gradient (ΔC) is depicted with a black line, where ($\Delta C = p\text{CO}_{2\text{water}} -$
 198 $p\text{CO}_{2\text{air}}$).
 199

200 Given the 3-year time series and strong diel cycling of $p\text{CO}_{2\text{water}}$ (and DO, see Fig. S1) in the
 201 Rhode River, we chose to aggregate aqueous minute-over-minute measurements to mean hourly
 202 measurements. Owing to the relative lack of short-term variability in local atmospheric CO_2
 203 concentrations (Fig. 2), we used linear interpolation to impute atmospheric CO_2 concentrations
 204 during hours in between actual readings (6-hour gaps between atmospheric measurements),
 205 which we assumed to be more realistic and reliable than Last Observation Carried Forward
 206 (LOCF) methods, where the last observation is repeated for all gaps until the next measurement
 207 is encountered, a method that has fallen out of favor, especially for environmental time series
 208 data (Lachin, 2016). To determine if any inadvertent bias was introduced by the linear
 209 interpolation procedure, summary statistics of actual atmospheric readings to actual readings +



210 imputed CO₂ values were compared statistically. This approach enabled us to take advantage of
211 >25,000 time points throughout the 3-year period of observation, providing hourly resolution.

212

213 2.2.3 CO₂ gradient (ΔC)

214 ΔC was determined by subtraction, $p\text{CO}_{2\text{water}} - p\text{CO}_{2\text{air}}$, where positive ΔC values correspond to
215 higher CO₂ concentrations in the water, tending toward movement from water to air (outgassing,
216 where Rhode River = CO₂ source), and negative values that signal CO₂ movement from air to
217 water transport (dissolution, where Rhode River = CO₂ sink). Values of $p\text{CO}_{2\text{water}}$, $p\text{CO}_{2\text{air}}$, and
218 ΔC are plotted on an hourly basis for the 3-year period beginning 01 July 2018 and ending 01
219 July 2021 (Fig. 2).

220

221 2.2.4 Accuracy of CO₂ measurements

222 Estimated accuracy of the spherical falling film equilibrator and NDIR sensor (SenseAir K30,
223 <https://senseair.com/>) combination were experimentally determined in the lab and found to
224 measure water equilibrated with known gas concentrations to be within the $\pm 1\%$ uncertainty
225 limits of the certified standard gas mixtures used and well within the published accuracy
226 specification of the SenseAir K30 (i.e., ± 30 ppmv $\pm 3\%$ of instrument reading). Experimental
227 analysis by Martin et al. (2017) report even higher accuracy when relative humidity and
228 atmospheric pressure are controlled for. Details on performance of the spherical falling film
229 equilibrator, such as accuracy, precision, and time constants can be found in Miller et al. (2019).
230 Although SenseAir offers automated calibration via long term comparisons to atmospheric
231 readings, this feature was deactivated. The K30 NDIR was periodically validated using standard
232 zero CO₂ (nitrogen) and standard certified span gases at intervals of one to two months during
233 the study period. Although the K30 was never observed to drift beyond its factory specifications,
234 the sensor was occasionally re-calibrated in the lab, and measured values were accepted without
235 adjustment.

236

237 CO₂ measurements were loaded into a database at approximately two-week intervals during the
238 observation period. Data were graphed and reviewed visually, in combination with twice weekly
239 observations of equilibrator function recorded in an accompanying notebook. Anomalous data



240 were flagged and excluded from data analysis (e.g., flooding or clogging events that interrupted
241 proper equilibration.)

242

243 2.3 Co-located water quality and atmospheric measurements

244 The water quality station at the SERC dock is a long-term node of the Maryland Department of
245 Natural Resources “Eyes on the Bay” Chesapeake Bay tidal water monitoring program, and has
246 been operated by the SERC since 1986. Water quality and atmospheric data are maintained by
247 the MarineGEO Upper Chesapeake Bay Observatory and can be accessed online (Benson et al.,
248 2023). A YSI EXO2 sonde is positioned 1 m below the water’s surface and in proximity (~2.5 m
249 distance) to the submerged water pump that feeds the $p\text{CO}_2$ equilibrator. Sonde measurements
250 were made at 6-minute intervals and aggregated to 1-hour mean values. The published accuracy
251 specifications for the YSI sonde are as follows: temperature: $\pm 0.01^\circ\text{C}$ (-5° to 35°); Salinity: $\pm 1\%$
252 of reading or 0.1 ppt (0–70 ppt); dissolved oxygen: ± 0.1 mg/L or 1% of reading (0 to 20 mg/L).
253 Discrete water samples were taken approximately weekly from the equilibrator feed water to
254 evaluate total alkalinity, and temperature and salinity measurements were made with a handheld
255 YSI Professional Plus 2030 with Quattro Cable instrument (specifications: temperature: $\pm 0.02^\circ\text{C}$
256 (-5°C to 70°C); salinity: $\pm 1\%$ of reading or 0.1 ppt (0–70 ppt); dissolved oxygen: ± 0.2 mg/L or
257 2% of reading (0 to 20 mg/L)). An equilibrator temperature probe was also co-located near the
258 intake of the equilibrator water pump and measured at 1-min intervals (EDS model OW-TEMP-
259 B3-12xA). Temperature: $\pm 0.5^\circ\text{C}$ (-10°C to 85°C). Discrete measurements were routinely
260 compared with the sonde to ensure measurement agreement. Wind speed measurements were
261 made using a sonic anemometer (Vaisala WXT-520 weather transmitter) mounted 7 m above the
262 mean low tide height of the water and located directly above the $p\text{CO}_2$ equilibrator.

263

264 2.4 Data Processing

265 Data included in this study spanned 01 Jul 2018 to 01 Jul 2021.

266

267 2.4.1 Gas-specific solubility

268 To determine the purely physical effects of temperature and salinity on CO_2 solubility, gas-
269 specific solubility values K_0 ($\text{mmol} \cdot \text{m}^{-3} \cdot \mu\text{atm}^{-1}$) were calculated across the 3-year observation



270 period using water temperature and salinity measurements in combination with $p\text{CO}_{2\text{water}}$ values,
271 according to Weiss and Price (1980) at 1-hour intervals.

272

273 2.4.2 Gas transfer velocity estimation (k)

274 Given the similarities between the Rhode River and New River estuaries (e.g., shallow,
275 microtidal estuaries with slow water velocity and strong diel cycles in $p\text{CO}_2$ and DO), we chose
276 to parameterize gas transfer velocity k ($\text{cm} \cdot \text{h}^{-1}$) standardized to the unitless Schmidt number
277 600 (k_{600}) according to the estuary-specific k parameterization model developed by Van Dam et
278 al. (2019) for shallow, microtidal estuaries. Van Dam et al. (2019) determined that k correlated
279 with wind speed differently during the daytime versus nighttime hours (linear vs. parabolic
280 relationships). Wind speed data were collected during the 3-year period from a sonic
281 anemometer located on the SERC dock directly above the equilibration system and
282 approximately 7 m above the water's surface at mean low tide height. For the analysis,
283 windspeeds were standardized for a height of 10 m following a power-law relationship, $U_{10} =$
284 $U_7 * (10/7)^{0.15}$ (Saucier, 2003). Wind speed data were binned to 1.5 m s^{-1} intervals for day and
285 night readings and raw values replaced by the mean wind speed for each bin. The median binned
286 windspeed over the Rhode River was 2.2 m s^{-1} , regardless of time of day or season. Recorded
287 windspeeds never exceeded 10 m/s and were dominated by much lower values (Fig. S1). Unlike
288 the New River Estuary, the Rhode River's windspeed profile does not differ much between day
289 and night, nor across season. For this reason, we chose to use the most conservative k_{600}
290 formulation from Van Dam et al. (2019), that combines day and night winds to estimate k_{600} .

291

292 Wind speed was used to parameterize k_{600} as follows:

293

$$294 \quad k_{600} = 1.5 * U_{10} + 4.2 \quad (2)$$

295

296 where U_{10} = mean of binned wind speed at 10 m above the water's surface ($\text{m} \cdot \text{s}^{-1}$).



297 2.4.3 CO₂ flux

298 Using continuous, parallel 3-year records (01 July 2018 to 01 July 2021) of dissolved and
299 atmospheric $p\text{CO}_2$, water temperature, salinity, and wind speed, CO₂ flux was derived according
300 to the equation:

301

$$302 \quad \text{CO}_2 \text{ flux} = k_{600} \cdot K_0 \cdot \Delta C \cdot (600 / Sc)^{-0.5} \quad (3)$$

303 where,

304 CO₂ flux = the rate and direction of CO₂ mass moving between water and gas phases

305 ($\text{mmol} \cdot \text{m}^{-2} \cdot \text{hr}^{-1}$)

306 k_{600} = gas transfer velocity ($\text{cm} \cdot \text{hr}^{-1}$), normalized to a common Schmidt number

307 ($Sc = 600$)

308 K_0 = gas-specific solubility for CO₂ ($\text{mmol} \cdot \text{m}^{-3} \cdot \mu\text{atm}^{-1}$)

309 ΔC = air-water concentration gradient (μatm)

310 Sc = Schmidt number

311

312 Note: CO₂ flux calculations require conversion from traditional k_{600} units ($\text{cm} \cdot \text{hr}^{-1}$) to ($\text{m} \cdot \text{hr}^{-1}$)
313 and from ΔC units (μatm) to (atm) prior to calculation.

314

315 2.4.4 Day/Night Designation

316 To differentiate daytime from nighttime hours, we used the position of the measurements
317 (latitude) in the Rhode River, combined with the local date and time. This approach enabled us to
318 uniformly designate various environmental measurements as happening during the day or night
319 (R package "LakeMetabolizer", Winslow et al., 2016).

320

321 2.4.5 Seasonality

322 We chose to break the year into two 6-month periods based on seasonal water temperature shifts,
323 designating June–November as “warm-water months” and Dec–May as “cold-water months”
324 (Fig. S1).



325 2.4.6 Effect size

326 Owing to the large number of observations available for comparison in this study, the likelihood
327 of finding statistically significant results is quite high. Whether such statistical results by
328 themselves connote practical and informative differences can be difficult to discern. So, effect
329 sizes (Omega-squared, ω^2) were calculated according to two-factor ANOVAs where independent
330 variables were investigated by season (cold-water vs. warm-water season), day/night period and
331 the interaction of season and day/night. The independent variables compared were: K_0 , CO_2 flux,
332 $\Delta p\text{CO}_2$, k_{600} , $p\text{CO}_{2\text{air}}$, $p\text{CO}_{2\text{water}}$, and wind speed. To account for temporal autocorrelation and
333 lack of independence of observations that are typical of environmental time series data, we
334 corrected for overinflation in the residual mean square used in the effect size calculations by
335 removing the autocorrelation present within residuals, leaving the white-noise component as the
336 unbiased estimate of residual variability (Cochrane-Orcutt procedure, R package "orcutt", Spada
337 et al., 2018).

338

339 **3. Results and Discussion**

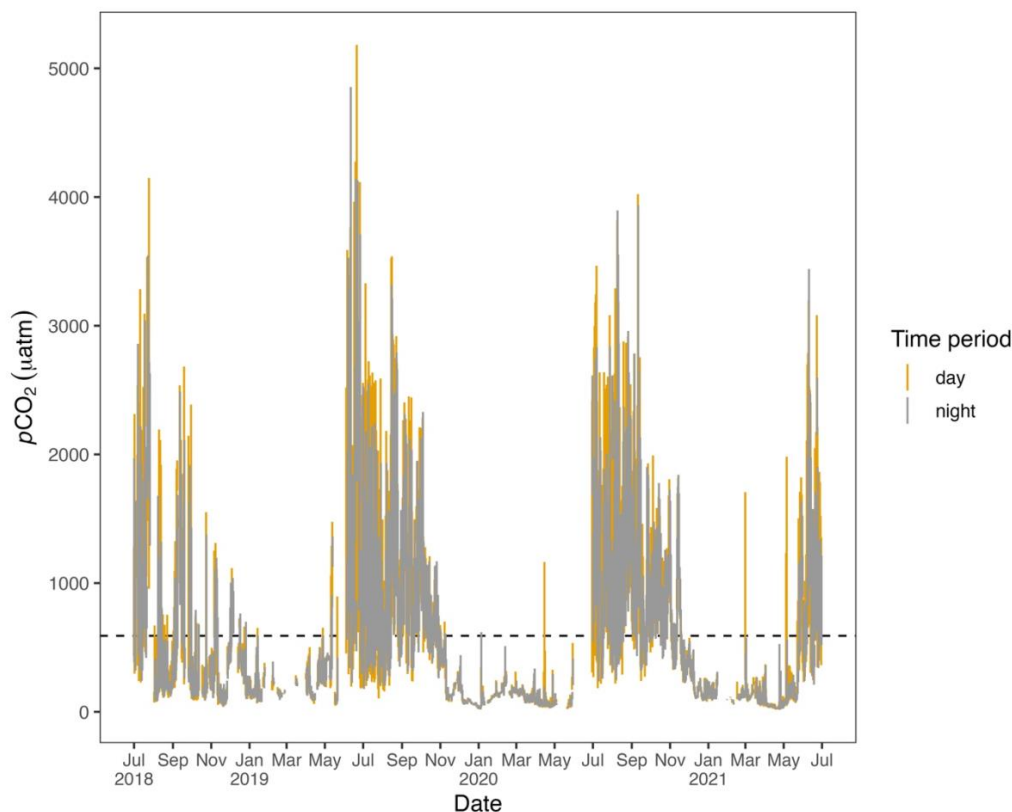
340 3.1 Daily and Seasonal Cycling of $p\text{CO}_2$

341 Hourly averaged measurements of $p\text{CO}_{2\text{water}}$ in the Rhode River across three years revealed
342 strong diel and seasonal cycling (Fig. 2). Mean and maximum $p\text{CO}_{2\text{water}}$ were significantly higher
343 in warm-water vs. cold-water months (Table 1). During warm-water months (June–Nov) daily
344 oscillations of $p\text{CO}_2$ frequently transit from far above to below ambient atmospheric conditions
345 over the course of the day, only to reverse direction (from low to high) during the nighttime
346 hours (Fig. 3). During the summer, $p\text{CO}_{2\text{water}}$ levels sometimes shifted by as much as 4500 μatm
347 in both directions during a single 24-hour period (Fig. 3). This pattern is consistent with
348 biologically driven cycling whereby very high early morning $p\text{CO}_{2\text{water}}$ conditions are depleted
349 by net photosynthetic activity (inorganic carbon fixation) over the course of the day, but high
350 $p\text{CO}_{2\text{water}}$ is restored by respiration in the benthos and water column at night (Song et al., 2023).
351 Comparing dissolved oxygen (DO) over the same period, similar harmonic cycling is observed,
352 but maximums and minimums of $p\text{CO}_2$ and DO were inversely related (Fig. S1), hallmarks of a
353 production/respiration driven system (Herrmann et al., 2020; Van Dam et al., 2019).



354 **Table 1.** Descriptive statistics comparing seasonality of $p\text{CO}_2$, CO_2 flux and associated
 355 parameters in cold-water (Dec–May) and warm-water seasons (June–Nov).
 356

Season	Time Period	Variable	Units	N	Mean	Min	Max	SD
overall	-	CO_2 flux	$\text{mmol} \cdot \text{m}^{-2} \cdot \text{hr}^{-1}$	20971	-0.091	-4.885	11.177	1.823
cold	day	CO_2 flux	$\text{mmol} \cdot \text{m}^{-2} \cdot \text{hr}^{-1}$	4494	-1.390	-4.885	8.264	1.134
cold	night	CO_2 flux	$\text{mmol} \cdot \text{m}^{-2} \cdot \text{hr}^{-1}$	5050	-1.388	-4.661	5.237	0.927
warm	day	CO_2 flux	$\text{mmol} \cdot \text{m}^{-2} \cdot \text{hr}^{-1}$	6007	1.183	-3.949	11.177	1.731
warm	night	CO_2 flux	$\text{mmol} \cdot \text{m}^{-2} \cdot \text{hr}^{-1}$	5421	0.781	-3.973	8.052	1.467
overall	-	K_0	$\text{mmol} \cdot \text{m}^{-3} \cdot \mu\text{atm}^{-1}$	20971	0.042	0.027	0.071	0.011
cold	day	K_0	$\text{mmol} \cdot \text{m}^{-3} \cdot \mu\text{atm}^{-1}$	4494	0.050	0.032	0.071	0.009
cold	night	K_0	$\text{mmol} \cdot \text{m}^{-3} \cdot \mu\text{atm}^{-1}$	5050	0.052	0.032	0.070	0.008
warm	day	K_0	$\text{mmol} \cdot \text{m}^{-3} \cdot \mu\text{atm}^{-1}$	6007	0.034	0.027	0.063	0.007
warm	night	K_0	$\text{mmol} \cdot \text{m}^{-3} \cdot \mu\text{atm}^{-1}$	5421	0.036	0.027	0.065	0.008
overall	-	k_{600}	$\text{cm} \cdot \text{hr}^{-1}$	20971	7.859	5.574	18.356	2.047
cold	day	k_{600}	$\text{cm} \cdot \text{hr}^{-1}$	4494	8.705	5.574	16.326	2.251
cold	night	k_{600}	$\text{cm} \cdot \text{hr}^{-1}$	5050	7.738	5.574	18.356	2.081
warm	day	k_{600}	$\text{cm} \cdot \text{hr}^{-1}$	6007	7.923	5.574	18.356	1.868
warm	night	k_{600}	$\text{cm} \cdot \text{hr}^{-1}$	5421	7.200	5.574	18.356	1.751
overall	-	ΔC	μatm	20971	154.002	-435.578	4749.504	645.758
cold	day	ΔC	μatm	4494	-238.871	-435.578	1553.228	220.859
cold	night	ΔC	μatm	5050	-256.124	-434.391	1204.023	164.172
warm	day	ΔC	μatm	6007	569.999	-399.477	4749.504	745.491
warm	night	ΔC	μatm	5421	402.784	-411.853	4401.171	628.229
overall	-	$p\text{CO}_{2\text{air}}$	μatm	20971	436.533	386.667	499.889	20.018
cold	day	$p\text{CO}_{2\text{air}}$	μatm	4494	429.909	389.648	496.667	16.025
cold	night	$p\text{CO}_{2\text{air}}$	μatm	5050	432.078	387.000	498.556	17.807
warm	day	$p\text{CO}_{2\text{air}}$	μatm	6007	439.103	389.648	499.444	20.668
warm	night	$p\text{CO}_{2\text{air}}$	μatm	5421	443.326	386.667	499.889	21.459
overall	-	$p\text{CO}_{2\text{water}}$	μatm	20971	590.535	15.243	5182.226	651.816
cold	day	$p\text{CO}_{2\text{water}}$	μatm	4494	191.038	15.243	1982.228	220.933
cold	night	$p\text{CO}_{2\text{water}}$	μatm	5050	175.954	16.746	1637.523	163.888
warm	day	$p\text{CO}_{2\text{water}}$	μatm	6007	1009.103	46.897	5182.226	752.634
warm	night	$p\text{CO}_{2\text{water}}$	μatm	5421	844.110	37.773	4854.949	632.244
overall	-	wind speed	$\text{m} \cdot \text{s}^{-1}$	20971	2.443	0.099	9.786	1.415
cold	day	wind speed	$\text{m} \cdot \text{s}^{-1}$	4494	3.055	0.278	8.904	1.525
cold	night	wind speed	$\text{m} \cdot \text{s}^{-1}$	5050	2.357	0.255	9.099	1.448
warm	day	wind speed	$\text{m} \cdot \text{s}^{-1}$	6007	2.497	0.146	9.786	1.277
warm	night	wind speed	$\text{m} \cdot \text{s}^{-1}$	5421	1.954	0.099	9.050	1.225



357

358 **Fig. 3.** Daily range of $p\text{CO}_2$ measurements categorized by readings taken during the day (yellow)
359 or night (gray). Note extensive range overlap among days and nights, illustrating the daily
360 oscillation from high to low values during day and low to high values at night. Horizontal line
361 indicates grand mean of hourly $p\text{CO}_2$ (= 591 μatm) over three years.

362

363 On the seasonal timescale, $p\text{CO}_2$ was consistently lowest and DO highest during cold-water
364 months of the year (Dec–May; Fig. S1). Importantly, for both gases the short-term temporal
365 variability (diel cycling) was most constrained during cold-water months across years, strongly
366 suggesting that carbon fixation exceeds respiration for prolonged periods (weeks to months). In
367 contrast, during warm-water months (Jun–Nov), photosynthesis/carbon fixation and respiration



368 are more evenly balanced, compensating for one another over 24-hour periods (i.e., respiration >
369 productivity at night and productivity > respiration during daylight hours; Fig. 3).

370

371 3.2 Air-water concentration gradient = ΔC (μatm)

372 When hourly $p\text{CO}_{2\text{water}}$ and $p\text{CO}_{2\text{air}}$ values (composed of 4 hourly measurements and 20
373 interpolated values per day) were plotted across the three years of observation, the diel and
374 seasonal cycles of $p\text{CO}_{2\text{water}}$ are evident. As expected, atmospheric concentrations of CO_2
375 remained relatively constant compared with aqueous loads. When the mean raw $p\text{CO}_{2\text{air}}$
376 measurements (mean = 435.1, 95% CI [434.4, 435.7]) were compared with raw $p\text{CO}_{2\text{air}}$
377 measurements + imputed estimates (mean = 435.4, 95% CI [435.2, 435.7]) no statistical
378 difference was observed, indicating that no substantial bias was introduced by linear
379 interpolation of atmospheric measurements.

380

381 Although nearshore atmospheric CO_2 concentrations are expected to vary more than those in
382 isolated well-mixed atmosphere (e.g., Mona Loa Observatory), annual mean values were
383 consistent and within the published uncertainty of the K30 NDIR sensor, when compared with
384 global measurements conducted at Mona Loa (Thoning et al., 2023). Variability at the 6-hour
385 measurement scale was considerable, reflecting expected local perturbations (e.g., effects of
386 terrestrial photosynthetic drawdown when wind is absent), yet there were no instances when the
387 measured local atmospheric values were suspiciously high or low for days on end, as compared
388 with expected global mean atmospheric values for the time period (i.e., 408–416 ppmv; Thoning
389 et al., 2023). This lack of sustained anomalous deviation served as additional confirmation that
390 the K30 sensor was functioning properly and had not drifted outside its calibration range.
391 Importantly, given the extreme diel cycling and seasonal variability of the Rhode River's
392 $p\text{CO}_{2\text{water}}$, the absolute accuracy necessary for determining year-over-year changes in
393 atmospheric or ocean $p\text{CO}_2$ is not a requirement for these CO_2 flux calculations which rely on
394 consistent, relative differences between water and atmospheric measurements.

395

396 Hourly air-water concentration gradient values = ΔC (μatm) were calculated and plotted across
397 the three years of study (Fig. 2). During warm months, $p\text{CO}_{2\text{water}}$ routinely shifts from
398 supersaturated to sub-atmospheric and back again, over the course of 24 hours (e.g., between

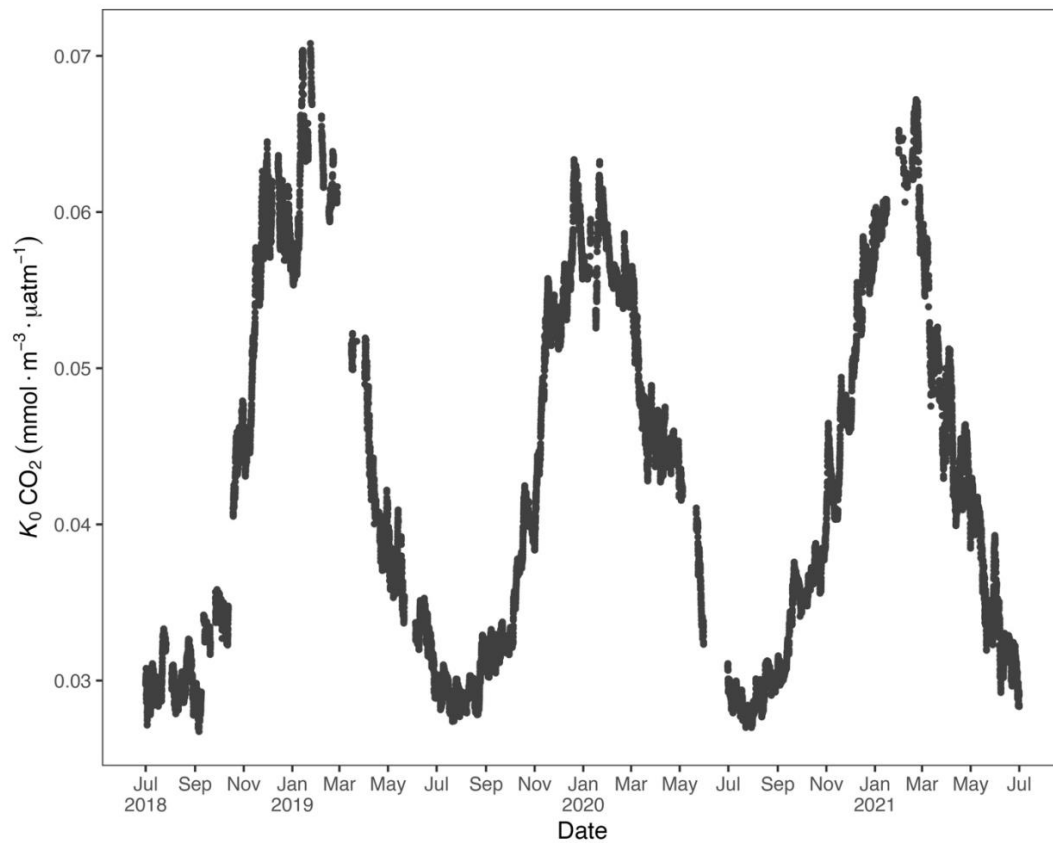


399 >2000 μatm and <410 μatm on a single day). These large daily swings in $p\text{CO}_{2\text{water}}$ produced
400 concomitant directional reversals of ΔC ($p\text{CO}_{2\text{water}} - p\text{CO}_{2\text{air}}$), which result in longer term
401 averaged gradients (e.g., multi-day, multi-week averages) near zero (Fig. 2). In contrast, the
402 majority of time during cold-water months is spent in a state of sub-atmospheric $p\text{CO}_{2\text{water}}$
403 (under-saturation with respect to the overlying atmosphere), resulting in ΔC values that are
404 negative, indicating movement of CO_2 from the atmosphere into the water over prolonged
405 periods.

406

407 3.3 Gas-specific solubility (K_0)

408 To account for the physical effects of temperature and salinity on the solubility of CO_2 in
409 estuarine water, the gas-specific solubility (K_0) was calculated by methods of Weiss and Price
410 (1980). K_0 varied strongly across seasons over the 3-year observation period. The maximum
411 annual range = 0.027 to 0.071 $\text{mmol} \cdot \text{m}^{-3} \cdot \mu\text{atm}^{-1}$. Mean cold-water months = 0.051 and mean
412 warm-water months = 0.035 $\text{mmol} \cdot \text{m}^{-3} \cdot \mu\text{atm}^{-1}$, confirming that CO_2 is most soluble in winter
413 and least soluble in summer (Fig. 4). This is inverse to observed dissolved CO_2 values: $p\text{CO}_{2\text{water}}$
414 was lowest and least variable during winter and highest and most variable during summer (Fig.
415 2, Table 1) suggesting that solubility, in and of itself, plays only a minor and non-limiting role in
416 determining $p\text{CO}_{2\text{water}}$ content in the Rhode River. Effect size (ω^2) estimates indicated that the
417 greatest proportion of variability in K_0 was associated with season, vs. day/night or the
418 interaction of the two (Table 2).



419

420 **Fig. 4.** Gas-specific solubility (K_0) for CO_2 based on water temperature and salinity.

421 Units are $\text{mmol m}^{-3} \mu\text{atm}^{-1}$ in the Rhode River (01 Jul 2018 to 01 Jul 2021)



422 **Table 2.** Contrast effect sizes based on two-factor ANOVA where independent variables were
 423 compared by season (cold-water season = Dec – May vs. warm-water season = June – Nov),
 424 day/night period and the interaction of the two. ω^2 is a measure of effect size, estimating the
 425 proportion of total variance explained by each parameter. Effect sizes were corrected for inherent
 426 temporal autocorrelation using the Cochran-Orcutt procedure (Spada et al., 2018).
 427

Variable	Factor	Effect Size (ω^2)
K_0	Season	0.0300
K_0	Day/Night	0.000575
K_0	Season:Day/Night	0.0000140
CO ₂ flux	Season	0.415
CO ₂ flux	Day/Night	0.00295
CO ₂ flux	Season:Day/Night	0.00301
ΔC	Season	0.310
ΔC	Day/Night	0.00501
ΔC	Season:Day/Night	0.00333
k_{600}	Season	0.00164
k_{600}	Day/Night	0.00269
k_{600}	Season:Day/Night	0.0000549
pCO_{2air}	Season	0.000137
pCO_{2air}	Day/Night	0.0000134
pCO_{2air}	Season:Day/Night	0.00000137
$pCO_{2\ water}$	Season	0.188
$pCO_{2\ water}$	Day/Night	0.00275
$pCO_{2\ water}$	Season:Day/Night	0.00191
wind speed	Season	0.00711
wind speed	Day/Night	0.0186
wind speed	Season:Day/Night	0.000182

428

429 3.4 Temperature/Biology ratio

430 To independently parse the magnitude of the physical versus biological forcing of pCO_{2water} , we
 431 estimated Takahashi’s Temperature/Biology ratio (Takahashi et al., 2002), a standardized
 432 approach to compare the influence of temperature and biological activities on pCO_{2water} . Across
 433 the 3-year period, we found that just $26.0 \pm 4.0\%$ (mean \pm SD) of forcing was attributable to
 434 temperature on solubility, confirming that the predominant driver of pCO_{2water} in the Rhode
 435 River is indeed biological activity (75%, Table 3). These patterns demonstrate the outsized role
 436 that biological processes play in shaping pCO_{2water} in nearshore marine and estuarine ecosystems
 437 (Dai et al., 2022; Van Dam et al., 2019).



438 **Table 3.** Takahashi Temperature/Biology Ratio (Eq. 5a From Takahashi et al. 2002).

439

Year	N	$\Delta p\text{CO}_2_{\text{bio}}$	$\Delta p\text{CO}_2_{\text{temp}}$	T/B ratio
2018	4416	3193.0	765.8	0.240
2019	8760	3669.8	1019.6	0.278
2020	8784	2772.1	846.0	0.305
2021	4345	2356.1	507.2	0.215
Overall	26305	3701.5	926.4	0.250

440

441

442 3.5 Gas transfer velocity (k_{600})

443 Gas transfer velocity is affected by both mass transfer by molecular diffusion driven by CO₂
 444 gradient between water and atmosphere and momentum transfer linked to external environmental
 445 forces that enhance turbulence at the air-water boundary layer (Ho et al., 2016; Raymond &
 446 Cole, 2001; Van Dam et al., 2019). Van Dam et al. (2019) validated the use of wind speed at 10
 447 m above the water’s surface (U_{10}) to estimate gas transfer velocities of CO₂ that were
 448 standardized to a Schmidt number of 600 (k_{600}) by comparing estimated values to k_{600} values
 449 derived directly from eddy covariance CO₂ flux measurements made in the New River Estuary,
 450 North Carolina, a shallow microtidal estuary similar to the Rhode River, which is applied here.
 451 Given the relative uniformity of wind speed over the Rhode River where median binned U_{10}
 452 windspeed (converted from U_7 measurements) was $2.2 \text{ m} \cdot \text{s}^{-1}$ regardless of time of day or
 453 season, and that maximum values rarely exceeded $10 \text{ m} \cdot \text{s}^{-1}$ (Table 1, Fig. S1), we chose to use
 454 the most conservative estuarine-specific parameterization of k_{600} (Van Dam et al., 2019) (Eq. 2).
 455 The mean overall Rhode River k_{600} value for CO₂ (mean \pm SD, $7.86 \pm 2.05 \text{ cm} \cdot \text{hr}^{-1}$) was of
 456 comparable magnitude to that of the New River Estuary ($9.37 \pm 9.47 \text{ cm} \cdot \text{hr}^{-1}$). Effect sizes (ω^2)
 457 indicate that season explained at least 10 times the observed variance than day/night or their
 458 interaction (Table 2). Given the minor freshwater input and microtidal nature of the Rhode River,
 459 we do not believe that lateral water velocity and bottom turbulence appreciably affect the gas
 460 transfer velocity of CO₂ here, although we did not investigate those possible influences
 461 explicitly.

462

463 Importantly, in coastal marine and estuarine habitats, ΔC can shift as much as several thousand
 464 μatm per day due to diel cycling associated with CO₂ production and depletion (Figs. 2 and 3).



465 The uncertainty surrounding gas transfer velocity parameterization can represent a major source
466 of error in CO₂ flux calculations (Frankignoulle et al., 1998; Upstill-Goddard, 2006; Wanninkhof
467 & McGillis, 1999); however, small errors in k_{600} have far less effect on CO₂ flux calculations in
468 estuaries which experience $p\text{CO}_2$ swings of several thousand μatm during a single day, compared
469 with more stable conditions of the open ocean where interannual ranges of $p\text{CO}_2$ are typically far
470 less (Van Dam et al., 2019).

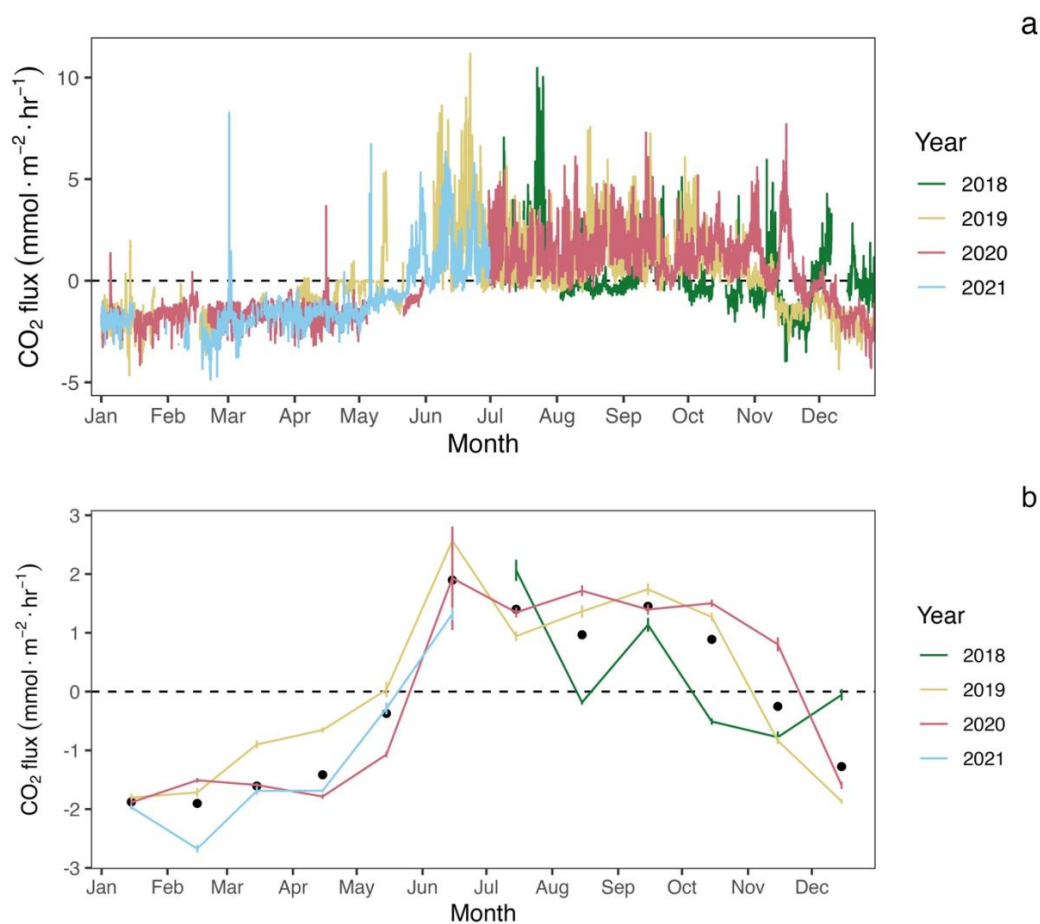
471

472 3.6 CO₂ flux - Seasonality and Interannual Variation

473 CO₂ flux was determined according to Eq. 3 using hourly ΔC measurements, CO₂ solubility
474 values (K_0) calculated according to temperature and salinity, and estuary-specific standardized
475 gas transfer velocities (k_{600}) of Van Dam et al. (2019). CO₂ flux was plotted across the three
476 years of observations at hourly and monthly intervals (Fig. 5a-b). As observed with $p\text{CO}_2$, CO₂
477 flux in the Rhode River was shown to be strongly seasonal. Given the apparent similarity in
478 windspeed across seasons (Fig. S1), the effect of differential mean ΔC and variation between
479 warm- and cold-water seasons (Fig. 2, Table 1) almost certainly drives the observed seasonal
480 differences in CO₂ flux (Fig. 5). Again, the specific solubility of CO₂ is greatest at low
481 temperatures, yet this is contrary to the observed mean $p\text{CO}_{2\text{water}}$ patterns, pointing toward a
482 biological mechanism for $p\text{CO}_2$, ΔC , and ultimately, CO₂ flux. The effect size of season on CO₂
483 flux was two orders of magnitude greater than either day/night or the season by day/night



484 interaction (Table 2).



485

486 **Fig. 5.** CO₂ flux estimates by year: a. Hourly, b. Monthly average CO₂ flux estimates with 95%
 487 confidence limits. Black dots in panel b indicate mean monthly fluxes across years.

488

489 Among years, $p\text{CO}_{2\text{water}}$ and CO₂ flux largely repeat themselves, with dissolved CO₂ becoming
 490 consistently sub-atmospheric and CO₂ flux going negative (gas exchange from atmosphere to
 491 water) between Dec and May and abruptly transitioning to much higher maximum, yet variable
 492 $p\text{CO}_{2\text{water}}$ values with net positive CO₂ fluxes from Jun through Nov (Figs. 1 and 5). Monthly
 493 averaged CO₂ fluxes are consistent among years (Fig. 5b), with net positive CO₂ fluxes
 494 (heterotrophic conditions) between June and November and negative (autotrophic) fluxes
 495 dominating when water temperatures are cold, between December and May. Despite the overall



496 similarities in seasonal CO₂ flux, inter-annual patterns can vary considerably. When hourly CO₂
497 flux values were averaged for the year, the Rhode River in 2019 was shown to have a net
498 positive flux but a net negative flux in 2020. When scaled for the year, 2019 outgassed CO₂ from
499 the water to the atmosphere at a rate of 2215.08 mmol · m⁻² · yr⁻¹ (95% CI = 1816.88, 2613.29).
500 The annual net flux rate in 2020 was negative (i.e. CO₂ moved from the atmosphere into the
501 river) at a rate of -1361.31 mmol · m⁻² · yr⁻¹ (95% CI = -1723.60, -999.01).

502

503 At shorter time scales, such as comparing the same week of the year among years, we sometimes
504 observed large differences in the magnitude and direction of CO₂ flux (Fig. S2), signaling
505 differences in seasonal conditions among years. Transient events can also result in deviations
506 from otherwise typical CO₂ flux conditions. For example, the period from July 2018 to Jan 2019
507 deviated from other years and CO₂ flux was more erratic, with intermittent episodes of negative
508 and positive CO₂ flux extending later into the winter season than in other years. When water
509 temperatures are compared among years, 2018 was shown to be more inconsistent, with more
510 pronounced temperature shifts and reversals than in 2019 or 2020 (Fig. S1). Salinities remained
511 relatively low for the latter half of 2018 into early 2019, reflecting wetter conditions (Fig. S1).
512 There were also two rapid salinity declines (>4 ppt reductions) in July and October 2018, likely
513 associated with strong precipitation events. These events were both followed by immediate
514 spikes in chlorophyll-*a* concentration to levels exceeding 200 µg · L⁻¹, indicative of
515 phytoplankton bloom conditions. From 2018 to 2021, chlorophyll-*a* levels of this magnitude and
516 greater were generally confined to cold-water months (Dec–May; Fig. S1). Erratic water
517 temperature and salinity are also reflected in more variable gas-specific solubility (*K*₀) for CO₂ in
518 2018 than later years (Fig. 4).

519

520 Gallegos et al. (1992) documented predictable phytoplankton blooms associated with freshets in
521 the Rhode River, when nutrient-rich freshwater inundates the estuary, not from point and non-
522 point sources within the local Rhode River watershed, but instead from the enormous watershed
523 that feeds the Susquehanna River, the primary source of freshwater input into the Chesapeake
524 above the Potomac as well as >50% of the entire Bay's freshwater (U.S. Geological Survey,
525 2023). Unlike river dominated estuaries, in the Rhode River estuary, volumetric influxes from
526 the Chesapeake Bay end member far exceed freshwater input from the Muddy Creek and



527 secondary tributaries. In the Rhode River, phytoplankton blooms result in the temporary
528 depletion of $p\text{CO}_{2\text{water}}$, followed by a spike, as phytoplankton senesce and organic carbon is
529 decomposed/re-mineralized back into inorganic carbon. Episodic, short-lived occurrences like
530 these demonstrate how immediate small scale biological forcing, can be coupled with, and
531 catalyzed by, distant large-scale weather and hydrological events. These in turn can influence
532 $p\text{CO}_2$ flux variations within seasons and among years (Fig. 5 and S2; and Chen et al., 2020).

533

534 Overall, except for wind speed, the effect sizes for the other six measured or calculated variables
535 were shown to be greatest for season, versus day/night or the interaction of season by day/night,
536 and in all cases the season effect was greater by at least 1 order of magnitude (Table 2).

537 Seasonality has 10 to 1000 times more explanatory power than other variables investigated as
538 estimated by ω^2 (Table 2).

539

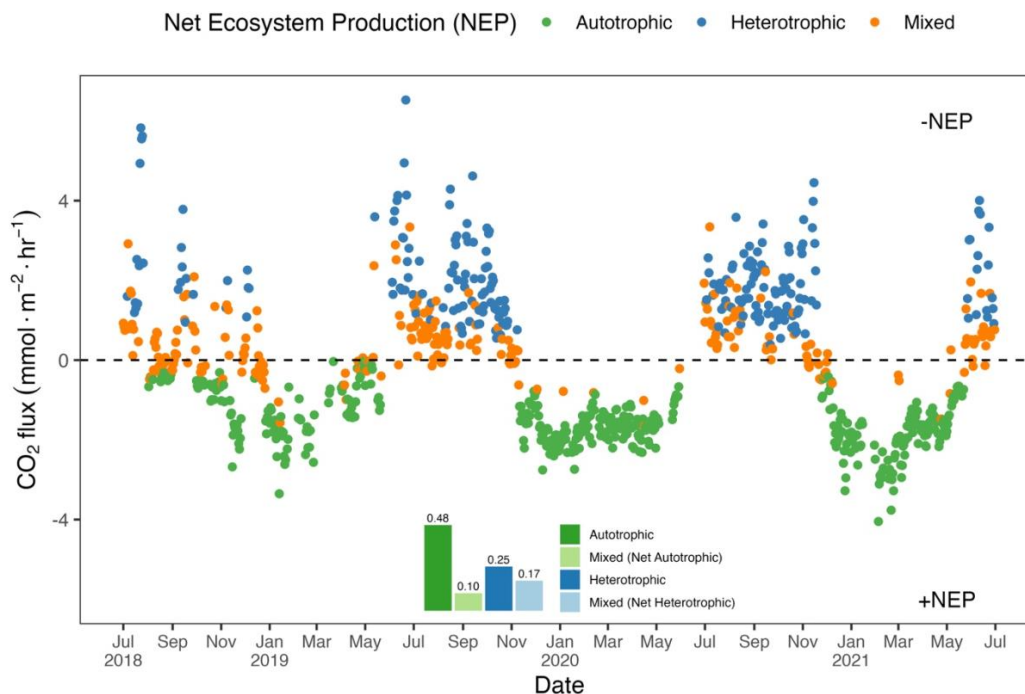
540 3.7 Diel Cycling

541 The notion that estuaries are predominantly heterotrophic systems that invariably outgas more
542 CO_2 to the atmosphere than they absorb has been a long-held view (Abril et al., 2000; Borges et
543 al., 2004; Cai, 2011; Cai et al., 2000; Chen, 2013; Frankignoulle et al., 1998, Gattuso et al.,
544 1998). However, more recently investigators have realized that physical and hydrological
545 characteristics, geographical location, size, and biological and biogeochemical activities may
546 individually, or together, influence CO_2 flux in estuaries and therefore contributions to
547 atmospheric chemistry (Brodeur et al., 2019; Caffrey, 2004; Chen et al., 2013, 2020; Herrmann
548 et al., 2020). Furthermore, inadequate sampling can induce bias (e.g., upscaling from a small
549 number of daytime samples taken during warm-water months can skew apparent patterns;
550 Laruelle et al., 2017; Van Dam et al., 2019.) Using 1-minute sampling intervals, averaged to the
551 hour continually over three years reveals patterns in the Rhode River that might otherwise be
552 overlooked. We document the Rhode River as having strong seasonality in both $p\text{CO}_2$ content as
553 well as the extent and direction of CO_2 flux (Figs. 2 and 3). Both measures are marked by daily
554 oscillations, frequently reversing the CO_2 gradient (ΔC) during a single 24-hour period in warm-
555 water months (Figs. 2 and 3) but are more stable and unidirectional during cold-water months
556 (Figs. 2 and 5).



557 3.8 Shifting Net Ecosystem Production

558 To better understand how the net ecosystem production (NEP) of the Rhode River shifts
559 throughout the year, where positive NEP indicates the river is storing carbon (autotrophic state)
560 and negative NEP indicates it is releasing carbon to the atmosphere (heterotrophic state), we
561 calculated hourly CO₂ flux values and averaged them by day (i.e. 24-hour period) and plotted
562 each in relation to the $\Delta C = 0$ reference. Each day of the 3-year study was categorized as either
563 net heterotrophic (CO₂ flux from water to atmosphere) or net autotrophic (CO₂ flux from
564 atmosphere to water). Each day was then further identified as either purely heterotrophic (all 24
565 hours were heterotrophic), purely autotrophic, or mixed (some hours were heterotrophic and
566 some were autotrophic, but resulting in a net autotrophic or net heterotrophic state for the day)
567 (Fig. 6). From July 2018 to July 2021, most 24-hour periods were categorized as pure
568 autotrophic ($444/920 = 48.3\%$), while 24.9% (229/990) were purely heterotrophic, and the
569 remainder of mixed trophic status (17.0% net heterotrophic and 10.0% net autotrophic; Fig. 6).



570

571 **Fig. 6.** Daily mean CO₂ flux estimates (CO₂ gradient is CO₂_{water} – CO₂_{air}). Green dots indicate
 572 days on which all 24 hrly flux measurements were negative (autotrophic with +NEP); blue dots
 573 indicate days on which all 24 hrly flux measurements were positive (heterotrophic with -NEP)
 574 and orange dots indicate that hourly fluxes were both negative or positive, and the position of the
 575 orange dot below or above the zero line indicates whether the day was net autotrophic or net
 576 heterotrophic. Insert describes the proportion of days in each category indicating that during
 577 58% (0.48 + 0.10) of days across three years of observation, the Rhode River was a CO₂ sink.
 578

579 Altogether, the Rhode River was net autotrophic for 58% of days (535 of 920 days) and net
 580 heterotrophic for 42% (385 days) across three years. However, because CO₂ flux is integrative, it
 581 is necessary to know the magnitude and direction of flux to understand the river’s composite
 582 NEP. When CO₂ flux is summarized across all 3 years, according to season and day/night cycles,
 583 the Rhode River estuary is shown to have near neutral NEP (Fig. 7). The effect size of season is
 584 two orders of magnitude greater than either that of day/night or season:day/night interaction
 585 (Table 2). Mean CO₂ flux values highlight the obvious correlation between season and NEP;
 586 error bars (± 1 SD) reveal the importance of diel cycling where the magnitude and directionality
 587 of Day/Night flux variability is approximately equal to the overall variability accrued across all



588 three years (Fig. 7). Although CO₂ flux is less variable and more autotrophic during cold-water
589 months than warm-months in the Rhode River, the range of possible values that occur across
590 night and day, regardless of season, must be taken into consideration to minimize incidental
591 sampling bias (Figs. 2 and 7).

592

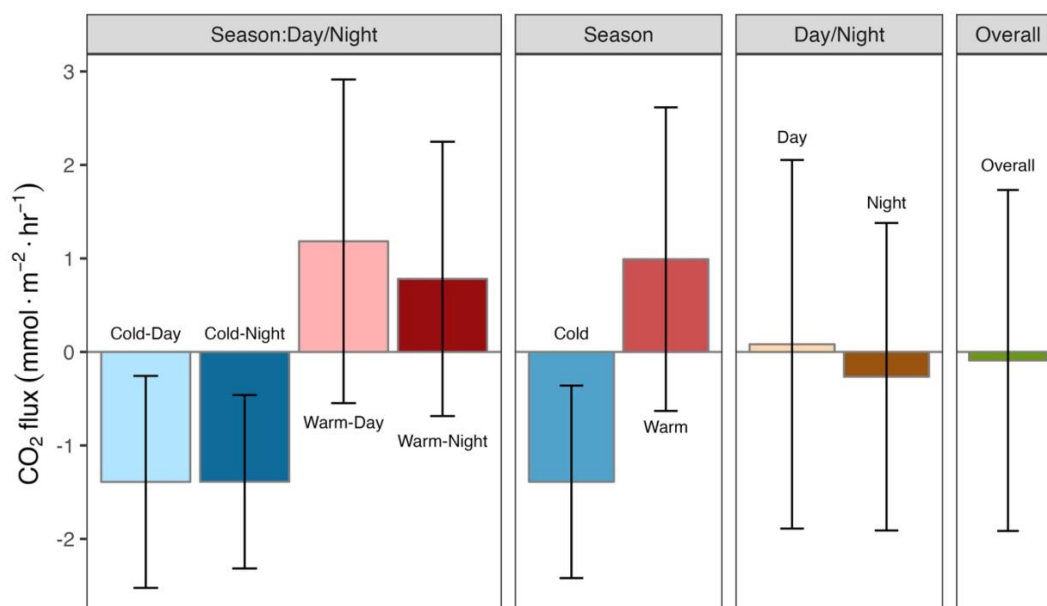
593 A multi-year investigation of CO₂ flux in the main stem of Chesapeake Bay by Chen et al.
594 (2020) combined several bay-wide cruises that were distributed across seasons to collect discrete
595 and underway *p*CO₂ data for CO₂ flux calculations. They concluded that the low salinity upper
596 bay, which receives large volumes of freshwater Susquehanna River, was net heterotrophic; the
597 mesohaline middle bay was net autotrophic, and the polyhaline lower bay was near carbon
598 neutral. Chen et al. (2020) characterized Chesapeake Bay, on the whole, as a weak source of CO₂
599 to the atmosphere (net flux = 0.73 mol · m⁻² · yr⁻¹) but suggested that during wet years, it may
600 function as weak sink of CO₂. Herrmann et al. (2020) also concluded that the Chesapeake Bay
601 was a weak source CO₂ to the atmosphere based on calculated *p*CO₂ values from long term pH
602 and alkalinity measurements (net flux = 1.2 mol · m⁻² · yr⁻¹mol). Brodeur and colleagues (2019)
603 examined DIC and total alkalinity along the mainstem of the Chesapeake Bay across the year in
604 2016 and concluded that DIC increases from north to south and from surface waters to depth and
605 that riverine input and biological cycling affect these values, however, concluding that the Bay
606 may be a net CO₂ sink.

607

608 When our annual mean *p*CO₂ values were compared with the Chen et al. (2020) survey, the
609 Rhode River was shown to be higher on average and more variable than the mesohaline main
610 stem of the bay (591 ± 652 vs. 416 ± 167 μatm), including a substantially greater measured range
611 (min = 15, max = 5182 μatm vs. 103 and 1033 μatm). These results suggest that water in the
612 shallow and well mixed Rhode River, and dissolved inorganic carbon (DIC) in particular,
613 undergo more acute biological transformation than in the mesohaline main stem of Chesapeake
614 Bay. Chen et al. (2020) point to a variety of factors that affect *p*CO₂ and CO₂ flux in the main
615 stem bay, including temperature, depth, stratification, and freshwater input volume, some of
616 which may attenuate biological forcing. Interannual variability was demonstrated in both the
617 Rhode River (some years were net autotrophic and others heterotrophic, Figs. 5 and 6) and in the
618 mesohaline main stem of the bay; however, we attribute interannual variability in *p*CO₂ and CO₂



619 flux primarily to variation in water temperature that in turn drives biological activity. We
 620 conclude that seasonal variations in the Rhode River (and likely similar rivers in the mesohaline
 621 portion of the Chesapeake) are significant and predictable, and that changes in pCO₂ and CO₂
 622 flux are associated with water temperature, which mediates NEP biologically, as opposed to
 623 changes in the solubility of CO₂.



624

625

626 **Fig. 7.** Mean CO₂ flux ± 1 SD (mmol · m⁻² · hr⁻¹) plotted by day/night cycling, cold-water/warm-
 627 water season, season by day/night interaction, and overall CO₂ flux.

628

629

630 3.9 Lateral transport

631 Tidal cycling has been shown to liberate and laterally transport DOC from brackish marshes to
 632 adjacent estuaries (Cai, 2011; Herrmann, 2015) and therefore is of great importance to carbon
 633 cycling and budgets of wetlands and estuaries (Najjar et al., 2020). DOC outwelling from the
 634 Kirkpatrick Marsh (hereafter KPM), a 21-ha tidal marsh located approximately 1 km up estuary
 635 from our primary study site at the SERC Dock (Fig. 1) into the Rhode River has been measured
 636 and modeled extensively in recent years (Clark et al., 2020; Menendez et al., 2022; Tzortziou et
 637 al., 2011; Tzortziou et al., 2008). These studies indicate that the KPM is responsible for a large



638 portion of overall DOC input to the Rhode River, as well as significant export from the river to
639 the mainstem of Chesapeake Bay. Model generation and validation by Clark et al. (2020)
640 indicate that up to 13.1% of the total DOC input to the Rhode River originates in the KPM.
641 Another important source (53% of total) is DOC derived from phytoplankton and is therefore
642 labile and readily biodegraded and remineralized into DIC. Furthermore, large quantities of
643 other, semi-labile forms of DOC are exported from the KPM, which are themselves subject to
644 photochemical and biodegradation and remineralization (Clark et al., 2020). Importantly, each of
645 these DOC streams provides a potential source of DIC, including $p\text{CO}_2$, to the Rhode River.
646
647 Dissolved inorganic carbon generated in brackish tidal wetlands is also outwelled directly into
648 estuaries (e.g., Cai et al., 2000; Chu et al., 2018; Song et al., 2023). Recent work by Song et al.
649 (2023) demonstrates that $p\text{CO}_2$ in a salt marsh tidal creek in Waquoit Bay, MA was regulated by
650 both tide height (inversely) and the day/night cycle, with nighttime low tides resulting in the
651 highest $p\text{CO}_2$ values, signaling a strong local effect from respiration and photosynthesis in
652 combination with tidal outwelling.
653
654 In the Rhode River watershed $p\text{CO}_2$ was measured continuously in the single tidal creek that
655 drains the KPM using the same methods as at our primary study location. We observed that the
656 KPM tidal creek $p\text{CO}_2$ follows the tidal cycle exclusively, yet outside the mouth of the tidal
657 creek, in the estuary proper, day/night cycling overwhelms this marsh tidal signal. Simultaneous
658 $p\text{CO}_2$ measurements from the SERC dock follows a strict day/night cycle (Fig. S3). However,
659 while peak levels of dissolved CO_2 in the Kirkpatrick Marsh creek occur at low tide and can
660 reach values nearly 20 times greater than highs at the SERC dock (Fig. S3) there is no obvious
661 evidence of this tidal signal at the dock site. These findings suggest that despite periodic extreme
662 CO_2 concentrations (>25,000 ppmv), the overall mass of CO_2 export is not sufficient to have an
663 immediate, measurable effects on the deeper, well-mixed portions of the Rhode River.
664 Remineralization of DOC exported from the KPM, as well as DOC originating in other locations
665 within the watershed are important sources of DIC in the river, but given the relative volumes of
666 these sources to that of the much larger estuary, as well as the physical distance (~1 km) from
667 SERC dock, these inputs are expected to undergo significant dilution effects, be partially off-
668 gassed to the atmosphere, and be metabolized via photosynthesis.



669 Thus, although land-sea interfaces and outwelling of DOC and DIC are important in estuaries
670 and coastal ecosystems, the relative sizes of wetlands and adjacent water bodies and the overall
671 volume of water moving between the two are also important factors. In eutrophic estuaries like
672 the Rhode River, biological forcing can rapidly assimilate DIC and degrade and mineralize labile
673 forms of DOC, as evidenced by extensive diel cycling in these systems (e.g., Brodeur et al.,
674 2019; Song et al., 2023, and the present study.) The much larger and complex Chesapeake Bay
675 generally follows seasonal changes in $p\text{CO}_2$ and CO_2 flux, but these appear to be most
676 predictable in the upper oligohaline portion and the polyhaline region of the bay near the mouth,
677 where freshwater and oceanic end-member effects are most pronounced (Brodeur et al., 2019;
678 Chen et al., 2020). The central mesohaline part of Chesapeake Bay comprises numerous discrete
679 and unique watersheds and subestuaries/rivers, each of which exchanges water with the bay.
680 Elucidating spatial and temporal patterns of $p\text{CO}_2$ and CO_2 flux are vital for understanding each
681 one's role as an atmospheric source or sink, but also could provide better insight into how each
682 may be influenced by global increases in atmospheric CO_2 (i.e., acidification and its influences
683 on estuarine metabolism, and the local biota, fisheries, and habitats.) Collectively, these and
684 other subestuaries will have cumulative effects on the overall water quality of Chesapeake Bay,
685 including cycling of DOC and DIC, which in turn affect $p\text{CO}_2$ and CO_2 flux.

686

687 **4. Conclusion and Recommendations**

688 As indicated in this study and others, the role that biological processes play in estuaries to either
689 fix CO_2 (autotrophy) or liberate CO_2 (heterotrophy) are extensive, complex, and can be quite
690 variable over space and time (Brodeur et al., 2019; Chen et al., 2020; Herrmann et al., 2020;
691 Rosentreter et al., 2021). High frequency automated measurements revealed strong seasonal
692 contrasts in dissolved CO_2 content and rates of CO_2 flux between water and atmosphere of the
693 Rhode River, a shallow mesohaline reach of the Chesapeake Bay. Importantly, only through high
694 frequency, multi-year measurements could diel and seasonal cycling be fully discerned. The
695 timing and frequency of measurements are critical and have potential for strong and misleading
696 biases if sampling is insufficient. In contrast, cold-water months coincide with long periods
697 (weeks to months) of continuous sub-atmospheric sink conditions for CO_2 . Using these
698 measurements, we estimated the direction and magnitude of CO_2 flux in hourly, daily, and
699 annual terms. In the Rhode River CO_2 flux reverses itself daily for part of the year (Jun–Nov)



700 yielding some days that are characterized as net sink (net autotrophic and $NEP > 0$) and others
701 that are net source (net heterotrophic and $NEP < 0$). From Dec–May diel cycling is minimal, and
702 the river is almost exclusively a sink/net autotrophic with +NEP both day and night. Although
703 CO_2 flux is pronounced but variable across seasons, the net CO_2 flux of the Rhode River on an
704 annual basis is near carbon neutral, although some years are net heterotrophic and others net
705 autotrophic.

706

707 High frequency sampling of pCO_2 , although typically confined spatially, is one approach to
708 understanding fundamental aspects of estuarine metabolic states and CO_2 flux that may
709 otherwise go undetected (Song et al., 2023). To address the spatial complexity of estuarine,
710 nearshore, and inland waters, more observation locations are required. As with any
711 environmental or ecological question, careful sampling design is critical to balance efficiency
712 and statistical power.

713

714 As the largest and arguably most complex estuary in the United States, the Chesapeake Bay is
715 the subject of extensive ecosystem management efforts and ranks among the most studied and
716 monitored estuaries in the world (Boesch & Goldman, 2009). Yet, information on CO_2 and
717 greenhouse gas flux continues to be limited (Brodeur et al., 2019; Chen et al., 2020; Herrmann et
718 al., 2020). Given the extensive coordinated monitoring programs that either make real-time water
719 quality measurements and/or maintain routine water sampling schedules (e.g., Maryland DNR
720 “Eyes on the Bay” program) in this region, strategic leveraging of existing water quality
721 observation assets and sampling programs could be achieved to more fully characterize and
722 quantify CO_2 and/or other greenhouse gas dynamics and flux in the Bay and elsewhere (see Saba
723 et al., 2019). For example, coordinated deployment of additional automated sampling devices
724 (e.g., robust air-water equilibrators and traditional atmospheric gas sensors) in key locations
725 would enable estimates of CO_2 flux, and if combined with pH, DIC, or total alkalinity
726 measurements, carbonate chemistry calculations as well. Importantly, such installations need not
727 be permanent. Instead, a small group of instruments could be systematically deployed across an
728 existing observation network, co-located with other water quality instruments using a stratified
729 sampling approach to capture spatial variability. For example, a set of shifting two-week to 1-
730 month long deployments during summer and winter months could yield sufficient data to



731 advance our understanding of Chesapeake Bay-wide CO₂ flux significantly in a single year. Such
732 information would complement underway transects which tend to underestimate temporal
733 variability in any given location. In the case of dissolved greenhouse gases, liquid-air
734 equilibration techniques are being used to measure multiple greenhouse gas gases (Call et al.,
735 2015; Gülzow et al., 2011; Hartmann, 2018; Miller et al., 2019; Xiao et al., 2020).

736

737 Understanding the greenhouse gas dynamics in estuaries is a vital component to generating
738 accurate global budgets (Maher & Eyre, 2012) as well as informing where emerging carbon
739 capture technologies might be best located (Bradshaw & Dance, 2005; Sun et al., 2021),
740 including nature-based solutions. In the case of estuaries, there have been extensive global losses
741 of seagrasses due to habitat degradation, pollution, and disease (Waycott et al., 2009). In addition
742 to many other ecosystem service benefits, restoration of seagrass and submerged aquatic
743 vegetation has the potential to restore and enhance natural carbon sequestration (i.e. blue carbon;
744 Kennedy et al., 2022; Macreadie et al., 2022; Unsworth et al., 2022). In an increasingly
745 automated world, marrying innovative, robust, and economical measurement solutions with
746 traditional observing networks will provide efficient, real-time information that can be readily
747 shared. Such information will increase our understanding of greenhouse gas flux at both the local
748 habitat scales that are of local ecological significance, as well as at the ecosystem level of an
749 estuary.

750

751 **Open Research**

752 The data used for analyses in this manuscript can be accessed at the following link:

753 https://smithsonian.figshare.com/articles/dataset/Hourly_means_of_data_used_in_the_manuscript

754 [t High frequency continuous measurements reveal strong diel and seasonal cycling of pC](#)

755 [O2 and CO2 flux in a mesohaline reach of the Chesapeake Bay /22491655](#)



756 **Author Contributions**

757 AWM conceptualized the study and was responsible for the acquisition of funding. ACR, MSM,
758 KJK, and AWM collected, managed, and curated data. JRM led formal analysis with
759 contributions from AWM and MSM. AWM and JRM prepared the original draft and all co-
760 authors edited and revised the manuscript.

761

762 **Competing Interests**

763 The authors declare that they have no conflict of interest.

764

765 **Acknowledgments**

766 We wish to thank Patrick Neale and Stephanie Wilson for their early review and critical
767 feedback on this manuscript, as well as J. Patrick Megonigal for discussions on methodology.
768 Funding for this research was provided by the Smithsonian Institution.

769

770 **References**

771

772 Abril, G., & Borges, A. V. (2005). Carbon Dioxide and Methane Emissions from Estuaries. In A.
773 Tremblay, L. Varfalvy, C. Roehm, & M. Garneau (Eds.), *Greenhouse Gas Emissions — Fluxes*
774 *and Processes: Hydroelectric Reservoirs and Natural Environments* (pp. 187–207). Berlin,
775 Heidelberg: Springer. https://doi.org/10.1007/978-3-540-26643-3_8

776

777 Abril, G., Etcheber, H., Borges, A. V., & Frankignoulle, M. (2000). Excess atmospheric carbon
778 dioxide transported by rivers into the Scheldt estuary. *Comptes Rendus de l'Académie Des*



- 779 *Sciences - Series IIA - Earth and Planetary Science*, 330(11), 761–768.
- 780 [https://doi.org/10.1016/S1251-8050\(00\)00231-7](https://doi.org/10.1016/S1251-8050(00)00231-7)
- 781
- 782 Bauer, J. E., Cai, W.-J., Raymond, P. A., Bianchi, T. S., Hopkinson, C. S., & Regnier, P. A. G.
- 783 (2013). The changing carbon cycle of the coastal ocean. *Nature*, 504(7478), 61–70.
- 784 <https://doi.org/10.1038/nature12857>
- 785
- 786 Benson, S., Rich, R., Tashjian, A., Lonneman, M., & Neale, P. (2023). MarineGEO Upper
- 787 Chesapeake Bay Observatory CPOP Data [Dataset]. Smithsonian Environmental Research
- 788 Center <https://doi.org/10.25573/SERC.C.6100368.V10>
- 789
- 790 Boesch, D.F., & Goldman, E.B. (2009). Chesapeake bay, USA. In K. McLeod & H. Leslie (Eds.)
- 791 *Ecosystem-Based Management for the Oceans* (pp. 268-293). Washington, D.C.: Island Press.
- 792
- 793 Borges, A. V. (2005). Do we have enough pieces of the jigsaw to integrate CO₂ fluxes in the
- 794 coastal ocean? *Estuaries*, 28(1), 3–27. <https://doi.org/10.1007/BF02732750>
- 795
- 796 Borges, A. V., Delille, B., Schiettecatte, L.-S., Gazeau, F., Abril, G., & Frankignoulle, M.
- 797 (2004). Gas transfer velocities of CO₂ in three European estuaries (Randers Fjord, Scheldt, and
- 798 Thames). *Limnology and Oceanography*, 49(5), 1630–1641.
- 799
- 800 Bradshaw, J., & Dance, T. (2005). Mapping geological storage prospectivity of CO₂ for the
- 801 world's sedimentary basins and regional source to sink matching. In *Greenhouse Gas Control*
- 802 *Technologies 7* (Vol. I, pp. 583–591). Elsevier. [https://doi.org/10.1016/B978-008044704-](https://doi.org/10.1016/B978-008044704-9/50059-8)
- 803 [9/50059-8](https://doi.org/10.1016/B978-008044704-9/50059-8)
- 804
- 805 Breitburg, D. L., Hines, A. H., Jordan, T. E., McCormick, M. K., Weller, D. E., & Whigham, D.
- 806 F. (2008). Landscape patterns, nutrient discharges, and biota of the Rhode River estuary and its
- 807 watershed: Contribution of the Smithsonian Environmental Research Center to the Pilot
- 808 Integrated Ecosystem Assessment. Edgewater, MD: Smithsonian Environmental Research



809 Center.

810

811 Brodeur, J.R.; Chen, B.; Su, J.; Xu, Y-Y; Hussain, N.; Scaboo, K.M.; Zhang, Y.; Testa, J.M. and

812 Cai, W.-J. (2019). Chesapeake Bay Inorganic Carbon: Spatial Distribution and Seasonal

813 Variability. *Front. Mar. Sci.* 6:99. doi: 10.3389/fmars.2019.00099

814

815 Broecker, W. S., Takahashi, T., Simpson, H. J., & Peng, T.-H. (1979). Fate of Fossil Fuel

816 Carbon Dioxide and the Global Carbon Budget. *Science*, 206(4417), 409–418.

817

818 Caffrey, J. M. (2004). Factors controlling net ecosystem metabolism in US estuaries. *Estuaries*,

819 27, 90–101.

820

821 Cai, W.-J. (2011). Estuarine and Coastal Ocean Carbon Paradox: CO₂ Sinks or Sites of

822 Terrestrial Carbon Incineration? *Annual Review of Marine Science*, 3(1), 123–145.

823 <https://doi.org/10.1146/annurev-marine-120709-142723>

824

825 Cai, W.-J., & Wang, Y. (1998). The chemistry, fluxes, and sources of carbon dioxide in the

826 estuarine waters of the Satilla and Altamaha Rivers, Georgia. *Limnology and Oceanography*,

827 43(4), 657–668. <https://doi.org/10.4319/lo.1998.43.4.0657>

828

829 Cai, W.-J., Wiebe, W. J., Wang, Y., & Sheldon, J. E. (2000). Intertidal marsh as a source of

830 dissolved inorganic carbon and a sink of nitrate in the Satilla River-estuarine complex in the

831 southeastern U.S. *Limnology and Oceanography*, 45(8), 1743–1752.

832 <https://doi.org/10.4319/lo.2000.45.8.1743>

833

834 Call, M., Maher, D. T., Santos, I. R., Ruiz-Halpern, S., Mangion, P., Sanders, C. J., et al. (2015).

835 Spatial and temporal variability of carbon dioxide and methane fluxes over semi-diurnal and

836 spring–neap–spring timescales in a mangrove creek. *Geochimica et Cosmochimica Acta*, 150,

837 211–225. <https://doi.org/10.1016/j.gca.2014.11.023>



- 838 Chen, B., Cai, W.-J., Brodeur, J. R., Hussain, N., Testa, J. M., Ni, W., & Li, Q. (2020). Seasonal
839 and spatial variability in surface pCO₂ and air–water CO₂ flux in the Chesapeake Bay.
840 *Limnology and Oceanography*, 65(12), 3046–3065. <https://doi.org/10.1002/lno.11573>
841
- 842 Chen, C.-T. A., Huang, T.-H., Chen, Y.-C., Bai, Y., He, X., & Kang, Y. (2013). Air–sea
843 exchanges of CO₂ in the world’s coastal seas. *Biogeosciences*, 10(10), 6509–6544.
844 <https://doi.org/10.5194/bg-10-6509-2013>
845
- 846 Chu, S. N., Wang, Z. A., Gonnee, M. E., Kroeger, K. D., & Ganju, N. K. (2018). Deciphering
847 the dynamics of inorganic carbon export from intertidal salt marshes using high-frequency
848 measurements. *Marine Chemistry*, 206, 7–18. <https://doi.org/10.1016/j.marchem.2018.08.005>
849
- 850 Clark, J. B., Long, W., & Hood, R. R. (2020). A Comprehensive Estuarine Dissolved Organic
851 Carbon Budget Using an Enhanced Biogeochemical Model. *Journal of Geophysical Research:*
852 *Biogeosciences*, 125(5), e2019JG005442. <https://doi.org/10.1029/2019JG005442>
853
- 854 Clark, J. B., Long, W., Tzortziou, M., Neale, P. J., & Hood, R. R. (2018). Wind-Driven
855 Dissolved Organic Matter Dynamics in a Chesapeake Bay Tidal Marsh-Estuary System.
856 *Estuaries and Coasts*, 41(3), 708–723. <https://doi.org/10.1007/s12237-017-0295-1>
857
- 858 Correll, D. L., Jordan, T. E., & Weller, D. E. (1992). Nutrient flux in a landscape: Effects of
859 coastal land use and terrestrial community mosaic on nutrient transport to coastal waters.
860 *Estuaries*, 15(4), 431–442. <https://doi.org/10.2307/1352388>
861
- 862 Dai, M., Su, J., Zhao, Y., Hofmann, E. E., Cao, Z., Cai, W.-J., et al. (2022). Carbon Fluxes in the
863 Coastal Ocean: Synthesis, Boundary Processes, and Future Trends. *Annual Review of Earth and*
864 *Planetary Sciences*, 50(1), 593–626. <https://doi.org/10.1146/annurev-earth-032320-090746>
865
- 866 Frankignoulle, M., Abril, G., Borges, A., Bourge, I., Canon, C., Delille, B., Libert, E., & Théate,
867 J.-M. (1998). Carbon Dioxide Emission from European Estuaries. *Science*, 282(5388), 434–436.
868 <https://doi.org/10.1126/science.282.5388.434>



869

870 Freeman, L. A., Corbett, D. R., Fitzgerald, A. M., Lemley, D. A., Quigg, A., & Steppe, C. N.

871 (2019). Impacts of urbanization and development on estuarine ecosystems and water quality.

872 *Estuaries and Coasts*, 42(7), 1821–1838. <https://doi.org/10.1007/s12237-019-00597-z>

873 Gallegos, C. L., Jordan, T. E., & Correll, D. L. (1992). Event-scale response of phytoplankton to

874 watershed inputs in a subestuary: Timing, magnitude, and location of blooms. *Limnology and*

875 *Oceanography*, 37(4), 813–828. <https://doi.org/10.4319/lo.1992.37.4.0813>

876

877 Gallegos, C. L., Jordan, T. E., & Hedrick, S. S. (2010). Long-term Dynamics of Phytoplankton

878 in the Rhode River, Maryland (USA). *Estuaries and Coasts*, 33(2), 471–484.

879 <https://doi.org/10.1007/s12237-009-9172-x>

880

881 Gattuso, J.-P., Frankignoulle, M., & Wollast, R. (1998). Carbon and Carbonate Metabolism in

882 Coastal Aquatic Ecosystems. *Annual Review of Ecology and Systematics*, 29(1), 405–434.

883 <https://doi.org/10.1146/annurev.ecolsys.29.1.405>

884

885 Gülzow, W., Rehder, G., Schneider, B., Deimling, J. S. v., & Sadkowiak, B. (2011). A new

886 method for continuous measurement of methane and carbon dioxide in surface waters using off-

887 axis integrated cavity output spectroscopy (ICOS): An example from the Baltic Sea. *Limnology*

888 *and Oceanography: Methods*, 9(5), 176–184. <https://doi.org/10.4319/lom.2011.9.176>

889

890 Hartmann, J. F.; Gentz, T.; Schiller, A.; Greule, M.; Grossart, H.-P.; Ionescu, D.; Keppler, F.;

891 Martinez-Cruz, K.; Sepulveda-Jauregui, A.; Isenbeck-Schröter, M. A. (2018). Fast and Sensitive

892 Method for the Continuous in Situ Determination of Dissolved Methane and Its $\delta^{13}\text{C}$ -Isotope

893 Ratio in Surface Waters. *Limnology and Oceanography: Methods* 16 (5):273–285.

894 <https://doi.org/10.1002/lom3.10244>.

895

896 Herrmann, M., Najjar, R. G., Da, F., Friedman, J. R., Friedrichs, M. A. M., Goldberger, S.,

897 Menendez, A., Shadwick, E. H., Stets, E. G., & St-Laurent, P. (2020). Challenges in Quantifying

898 Air-Water Carbon Dioxide Flux Using Estuarine Water Quality Data: Case Study for

899 Chesapeake Bay. *Journal of Geophysical Research: Oceans*, 125(7), e2019JC015610.



900 <https://doi.org/10.1029/2019JC015610>

901

902 Herrmann, M., Najjar, R. G., Kemp, W. M., Alexander, R. B., Boyer, E. W., Cai, W.-J., et al.
903 (2015). Net ecosystem production and organic carbon balance of U.S. East Coast estuaries: A
904 synthesis approach. *Global Biogeochemical Cycles*, 29(1), 96–111.

905 <https://doi.org/10.1002/2013GB004736>

906

907 Ho, D. T., Coffineau, N., Hickman, B., Chow, N., Koffman, T., & Schlosser, P. (2016).
908 Influence of current velocity and wind speed on air-water gas exchange in a mangrove estuary.
909 *Geophysical Research Letters*, 43(8), 3813–3821. <https://doi.org/10.1002/2016GL068727>

910

911 Jiang, L.-Q., Cai, W.-J., & Wang, Y. (2008). A comparative study of carbon dioxide degassing in
912 river- and marine-dominated estuaries. *Limnology and Oceanography*, 53(6), 2603–2615.

913 <https://doi.org/10.4319/lo.2008.53.6.2603>

914

915 Joesoef, A., Huang, W.-J., Gao, Y., & Cai, W.-J. (2015). Air–water fluxes and sources of carbon
916 dioxide in the Delaware Estuary: spatial and seasonal variability. *Biogeosciences*, 12(20), 6085–
917 6101. <https://doi.org/10.5194/bg-12-6085-2015>

918

919 Jordan, T. E., & Correll, D. L. (1991). Continuous automated sampling of tidal exchanges of
920 nutrients by brackish marshes. *Estuarine, Coastal and Shelf Science*, 32(6), 527–545.

921 [https://doi.org/10.1016/0272-7714\(91\)90073-K](https://doi.org/10.1016/0272-7714(91)90073-K)

922

923 Jordan, T. E., Correll, D. L., Miklas, J., & Weller, D. E. (1991). Nutrients and chlorophyll at the
924 interface of a watershed and an estuary. *Limnology and Oceanography*, 36(2), 251–267.

925 <https://doi.org/10.4319/lo.1991.36.2.0251>

926

927 Jordan, T. E., Correll, D. L., Peterjohn, W. T., & Weller, D. E. (1986). Nutrient flux in a
928 landscape: The Rhode River watershed and receiving waters. In D. L. Correll (Ed.), *Watershed*



- 929 *Research Perspectives*. Washington, DC: Smithsonian Institution Press. Retrieved from
930 <http://repository.si.edu/xmlui/handle/10088/17890>
931
- 932 Kennedy, H., Pagès, J. F., Lagomasino, D., Arias-Ortiz, A., Colarusso, P., Fourqrean, J. W., et
933 al. (2022). Species Traits and Geomorphic Setting as Drivers of Global Soil Carbon Stocks in
934 Seagrass Meadows. *Global Biogeochemical Cycles*, 36(10), e2022GB007481.
935 <https://doi.org/10.1029/2022GB007481>
936
- 937 Klaus, M., & Vachon, D. (2020). Challenges of predicting gas transfer velocity from wind
938 measurements over global lakes. *Aquatic Sciences*, 82(3), 53. [https://doi.org/10.1007/s00027-](https://doi.org/10.1007/s00027-020-00729-9)
939 [020-00729-9](https://doi.org/10.1007/s00027-020-00729-9)
940
- 941 Lachin, J. M. (2016). Fallacies of last observation carried forward analyses. *Clinical Trials*,
942 13(2), 161–168. <https://doi.org/10.1177/1740774515602688>
943
- 944 Laruelle, G. G., Goossens, N., Arndt, S., Cai, W.-J., & Regnier, P. (2017). Air–water CO₂
945 evasion from US East Coast estuaries. *Biogeosciences*, 14(9), 2441–2468.
946 <https://doi.org/10.5194/bg-14-2441-2017>
947
- 948 Macreadie, P. I., Robertson, A. I., Spinks, B., Adams, M. P., Atchison, J. M., Bell-James, J., et
949 al. (2022). Operationalizing marketable blue carbon. *One Earth*, 5(5), 485–492.
950 <https://doi.org/10.1016/j.oneear.2022.04.005>
951
- 952 Maher, D. T., & Eyre, B. D. (2012). Carbon budgets for three autotrophic Australian estuaries:
953 Implications for global estimates of the coastal air–water CO₂ flux. *Global Biogeochemical*
954 *Cycles*, 26(1). <https://doi.org/10.1029/2011GB004075>
955
- 956 Martin, C. R., Zeng, N., Karion, A., Dickerson, R. R., Ren, X., Turpie, B. N., & Weber, K. J.
957 (2017). Evaluation and environmental correction of ambient CO₂ measurements from a low-cost
958 NDIR sensor. *Atmospheric Measurement Techniques*, 10(7), 2383–2395.
959 <https://doi.org/10.5194/amt-10-2383-2017>



960

961 Menendez, A., Tzortziou, M., Neale, P., Megonigal, P., Powers, L., Schmitt-Kopplin, P., &
962 Gonsior, M. (2022). Strong Dynamics in Tidal Marsh DOC Export in Response to Natural
963 Cycles and Episodic Events From Continuous Monitoring. *Journal of Geophysical Research:*
964 *Biogeosciences*, 127(7), e2022JG006863. <https://doi.org/10.1029/2022JG006863>

965

966 Miller, A. W., Reynolds, A. C., & Minton, M. S. (2019). A spherical falling film gas-liquid
967 equilibrator for rapid and continuous measurements of CO₂ and other trace gases. *PLOS ONE*,
968 14(9), e0222303. <https://doi.org/10.1371/journal.pone.0222303>

969

970 Najjar, R. G., Herrmann, M., Cintrón Del Valle, S. M., Friedman, J. R., Friedrichs, M. A. M.,
971 Harris, L. A., et al. (2020). Alkalinity in Tidal Tributaries of the Chesapeake Bay. *Journal of*
972 *Geophysical Research: Oceans*, 125(1), e2019JC015597. <https://doi.org/10.1029/2019JC015597>

973

974 Raymond, P. A., & Cole, J. J. (2001). Gas Exchange in Rivers and Estuaries: Choosing a Gas
975 Transfer Velocity. *Estuaries*, 24(2), 312–317. <https://doi.org/10.2307/1352954>

976

977 Raymond, P. A., Hartmann, J., Lauerwald, R., Sobek, S., McDonald, C., Hoover, M., Butman,
978 D., Striegl, R., Mayorga, E., Humborg, C., Kortelainen, P., Dürr, H., Meybeck, M., Ciais, P., &
979 Guth, P. (2013). Global carbon dioxide emissions from inland waters. *Nature*, 503(7476), Article
980 7476. <https://doi.org/10.1038/nature12760>

981

982 Rose, K. C., Neale, P. J., Tzortziou, M., Gallegos, C. L., & Jordan, T. E. (2019). Patterns of
983 spectral, spatial, and long-term variability in light attenuation in an optically complex sub-
984 estuary. *Limnology and Oceanography*, 64(S1), S257–S272. <https://doi.org/10.1002/lno.11005>

985

986 Rosentreter, J. A., Wells, N. S., Ulseth, A. J., & Eyre, B. D. (2021). Divergent Gas Transfer
987 Velocities of CO₂, CH₄, and N₂O Over Spatial and Temporal Gradients in a Subtropical
988 Estuary. *Journal of Geophysical Research: Biogeosciences*, 126(10), e2021JG006270.

989



- 990 Saba, G. K., Goldsmith, K. A., Cooley, S. R., Grosse, D., Meseck, S. L., Miller, A. W., et al.
991 (2019). Recommended priorities for research on ecological impacts of ocean and coastal
992 acidification in the U.S. Mid-Atlantic. *Estuarine, Coastal and Shelf Science*, 225, 106188.
993 <https://doi.org/10.1016/j.ecss.2019.04.022>
994
- 995 [Saucier, W. J. \(2003\). *Principles of Meteorological Analysis*. Dover Publications.](#)
- 996
- 997 Song, S., Wang, Z. A., Kroeger, K. D., Eagle, M., Chu, S. N., & Ge, J. (2023). High-frequency
998 variability of carbon dioxide fluxes in tidal water over a temperate salt marsh. *Limnology and*
999 *Oceanography*. Spada, S., Quartagno, M., Tamburini, M., & Robinson, D. (2018). orcutt:
1000 Estimate Procedure in Case of First Order Autocorrelation (Version 2.3). Retrieved from
1001 <https://cran.r-project.org/web/packages/orcutt/index.html>
1002
- 1003 Sun, X., Alcalde, J., Bakhtbidar, M., Elío, J., Vilarrasa, V., Canal, J., et al. (2021). Hubs and
1004 clusters approach to unlock the development of carbon capture and storage – Case study in
1005 Spain. *Applied Energy*, 300, 117418. <https://doi.org/10.1016/j.apenergy.2021.117418>
1006
- 1007 Takahashi, T., Sutherland, S. C., Sweeney, C., Poisson, A., Metzl, N., Tilbrook, B., et al. (2002).
1008 Global sea–air CO₂ flux based on climatological surface ocean pCO₂, and seasonal biological
1009 and temperature effects. *Deep Sea Research Part II: Topical Studies in Oceanography*, 49(9),
1010 1601–1622. [https://doi.org/10.1016/S0967-0645\(02\)00003-6](https://doi.org/10.1016/S0967-0645(02)00003-6)
1011
- 1012 Thoning, K. W., Crotwell, A. M., & Mund, J. W. (2023). NOAA Global Monitoring Laboratory
1013 Carbon Cycle and Greenhouse Gases Group Continuous In situ Measurements of CO₂ at Global
1014 Background Sites, 1973–2022. (Version 2023-08-24) [Dataset]. National Oceanic and
1015 Atmospheric Administration (NOAA), Global Monitoring Laboratory (GML), Boulder,
1016 Colorado, USA. <https://doi.org/10.15138/YAF1-BK21>



- 1017 Tzortziou, M., Neale, P. J., Megonigal, J. P., Pow, C. L., & Butterworth, M. (2011). Spatial
1018 gradients in dissolved carbon due to tidal marsh outwelling into a Chesapeake Bay estuary.
1019 *Marine Ecology Progress Series*, 426, 41–56. <https://doi.org/10.3354/meps09017>
1020
- 1021 Tzortziou, M., Neale, P. J., Osburn, C. L., Megonigal, J. P., Maie, N., & Jaff , R. (2008). Tidal
1022 marshes as a source of optically and chemically distinctive colored dissolved organic matter in
1023 the Chesapeake Bay. *Limnology and Oceanography*, 53(1), 148–159.
1024 <https://doi.org/10.4319/lo.2008.53.1.0148>
1025
- 1026 Unsworth, R. K. F., Cullen-Unsworth, L. C., Jones, B. L. H., & Lilley, R. J. (2022). The
1027 planetary role of seagrass conservation. *Science*, 377(6606), 609–613.
1028 <https://doi.org/10.1126/science.abq6923>
1029
- 1030 Upstill-Goddard, R. C. (2006). Air–sea gas exchange in the coastal zone. *Estuarine, Coastal and*
1031 *Shelf Science*, 70(3), 388–404. <https://doi.org/10.1016/j.ecss.2006.05.043>
1032
- 1033 |U.S. Geological Survey (2023). Freshwater Flow into Chesapeake Bay. Retrieved September 28,
1034 2023, from [https://www.usgs.gov/centers/chesapeake-bay-activities/science/freshwater-flow-](https://www.usgs.gov/centers/chesapeake-bay-activities/science/freshwater-flow-chesapeake-bay)
1035 [chesapeake-bay](https://www.usgs.gov/centers/chesapeake-bay-activities/science/freshwater-flow-chesapeake-bay)
1036
- 1037 Van Dam, B. R., Edson, J. B., & Tobias, C. (2019). Parameterizing Air-Water Gas Exchange in
1038 the Shallow, Microtidal New River Estuary. *Journal of Geophysical Research: Biogeosciences*,
1039 124(7), 2351–2363. <https://doi.org/10.1029/2018JG004908>
1040
- 1041 Wanninkhof, R. (1992). Relationship between wind speed and gas exchange over the ocean.
1042 *Journal of Geophysical Research: Oceans*, 97(C5), 7373–7382.
1043
- 1044 Wanninkhof, R. (2014). Relationship between wind speed and gas exchange over the ocean
1045 revisited. *Limnology and Oceanography: Methods*, 12(6), 351–362.
1046 <https://doi.org/10.4319/lom.2014.12.351>



- 1047 Wanninkhof, R., & McGillis, W. R. (1999). A cubic relationship between air-sea CO₂ exchange
1048 and wind speed. *Geophysical Research Letters*, 26(13), 1889–1892.
1049 <https://doi.org/10.1029/1999GL900363>
1050
- 1051 Wanninkhof, R., Park, G.-H., Takahashi, T., Sweeney, C., Feely, R., Nojiri, Y., et al. (2013).
1052 Global ocean carbon uptake: magnitude, variability and trends. *Biogeosciences*, 10(3), 1983–
1053 2000. <https://doi.org/10.5194/bg-10-1983-2013>
1054
- 1055 Waycott, M., Duarte, C. M., Carruthers, T. J. B., Orth, R. J., Dennison, W. C., Olyarnik, S., et al.
1056 (2009). Accelerating loss of seagrasses across the globe threatens coastal ecosystems.
1057 *Proceedings of the National Academy of Sciences*, 106(30), 12377–12381.
1058 <https://doi.org/10.1073/pnas.0905620106>
1059
- 1060 Weiss, R., & Price, B. (1980). Nitrous oxide solubility in water and seawater. *Marine Chemistry*,
1061 8(4), 347–359. [https://doi.org/10.1016/0304-4203\(80\)90024-9](https://doi.org/10.1016/0304-4203(80)90024-9)
1062
- 1063 Winslow, L. A., Zwart, J. A., Batt, R. D., Dugan, H. A., Woolway, R. I., Corman, J. R., & Read,
1064 J. S. (2016). LakeMetabolizer: An R package for estimating lake metabolism from free-water
1065 oxygen using diverse statistical models. *Inland Waters: Journal of the International Society of*
1066 *Limnology*, 6(4). <https://doi.org/10.1080/IW-6.4.883>
1067
- 1068 Xiao, S., Liu, L., Wang, W., Lorke, A., Woodhouse, J., & Grossart, H.-P. (2020). A Fast-
1069 Response Automated Gas Equilibrator (FaRAGE) for continuous in situ measurement of CH₄
1070 and CO₂ dissolved in water. *Hydrology and Earth System Sciences*, 24(7), 3871–3880.
1071 <https://doi.org/10.5194/hess-24-3871-2020>
1072
- 1073 Zeebe, R. E., & Wolf-Gladrow, D. (2001). *CO₂ in Seawater: Equilibrium, Kinetics, Isotopes*.
1074 Gulf Professional Publishing.